

INFLUENCE OF ROTATION ON STELLAR EVOLUTION

A. Palacios¹

Abstract. The Sun has been known to rotate for more than 4 centuries, and evidence is also available through direct measurements, that almost all stars rotate. In this lecture, I will propose a review of the different physical processes associated to rotation that are expected to impact the evolution of stars. I will describe in detail the way these physical processes are introduced in 1D stellar evolution codes and how their introduction in the modelling has impacted our understanding of the internal structure, nucleosynthesis and global evolution of stars.

1 Foreword

In his Ph.D. thesis, published in 2012, Dr A. Potter writes a humoristic yet quite true sentence

Stars rotate because it is actually quite hard for them not to.

The molecular clouds that form stars are highly turbulent and part of their velocity dispersion is due to rotation. Although a substantial fraction of the total angular momentum should be lost during the collapse, the stars that are formed inherit angular momentum, and rotation is a natural feature among their characteristics (see P. Hennebelle and A. Belloche in this volume).

This fact being established conceptually and observationally (see § 2), the question that remains is whether rotation significantly affects the structure, evolution and nucleosynthesis of stars, and if so, how and to what extent.

These are the questions within the scope of this lecture, where I will briefly summarize the observational evidences of stellar rotation (§ 2), review the expected effects on the stellar structure and how they can be taken into account in stellar evolution modelling (§ 3). I will also describe the main transport mechanisms that could be driven by rotation in stellar interiors (§ 4) and how angular momentum evolution can be followed in stellar evolution codes (§ 5). In the last part (§ 6), I will present some key results obtained with rotating stellar evolution models.

¹ LUPM - UMR 5299 - CNRS/Université Montpellier II - cc 072 - Place Eugène Bataillon - F-34095 Montpellier (France)

2 Observational evidences of stellar rotation

2.1 Measurements of stellar rotation

The rotation of stars was first evidenced by Galileo Galilei (Galilei et al. 1613) in the case of the Sun, and in the late nineteenth - early twentieth century, the development of spectroscopy allowed astronomers to first envision to measure the rotation of stars by studying the broadening of the spectral lines that should result from it (Abney 1877, Monck 1890, Souleyre 1898, Fowler 1900).

Direct measurements of the rotation rate of stars are accessible via

- *photometry* light curve modulation by rotation allows to derive rotation periods P_{rot} ;
- *spectroscopy* spectral lines broadening is partly due to surface rotation and an estimation of the projected surface velocity on the line of sight, $v \sin i$ can be obtained from spectral analysis;
- *spectropolarimetry and Doppler imaging* modulation of the polarized signal by rotation allowing to derive rotation periods P_{rot} and surface latitudinal differential rotation $\delta\Omega$;
- *asteroseismology* splitting of oscillation modes due to rotation allows the reconstruction of the rotation profile of some stars in addition to the Sun;
- *interferometry* direct imaging of rapidly rotating non-spherical stellar surfaces allows to estimate the mean rotation rate as a fraction of the break-up velocity.

For some types of stars it is very difficult to actually derive a rotation rate, either because the spectral lines broadening is dominated by another process, as surface convection, which is the case of red giants and supergiants, or because the actual stellar surface is not accessible to observation, as it is the case for Wolf-Rayet stars, in which the dense winds yield the formation of spectral lines in the wind and not in the hydrostatic regions that could define an actual stellar surface, preventing any measurement of stellar rotation.

The rotational study of stars based on these measurements allows us to draw some sort of rotational HR diagram :

O and B-type stars (Fig. 1, ab):

$v \sin i$ measurements in the Galaxy and in the Magellanic Clouds indicate that these are rapidly rotating stars, with a mean projected velocity of about 130 km.s^{-1} for B-type stars (Bragança et al. 2012, Hunter et al. 2008b, Mokiem et al. 2006, Abt et al. 2002), and about 110 km.s^{-1} for O-type stars (Penny 1996, Penny & Gies 2009). Some stars in the O_n subtype (with nitrogen enrichment) can reach projected velocities of about 420 km.s^{-1} (Walborn et al. 2011) but the number of these very rapid rotators is actually limited.

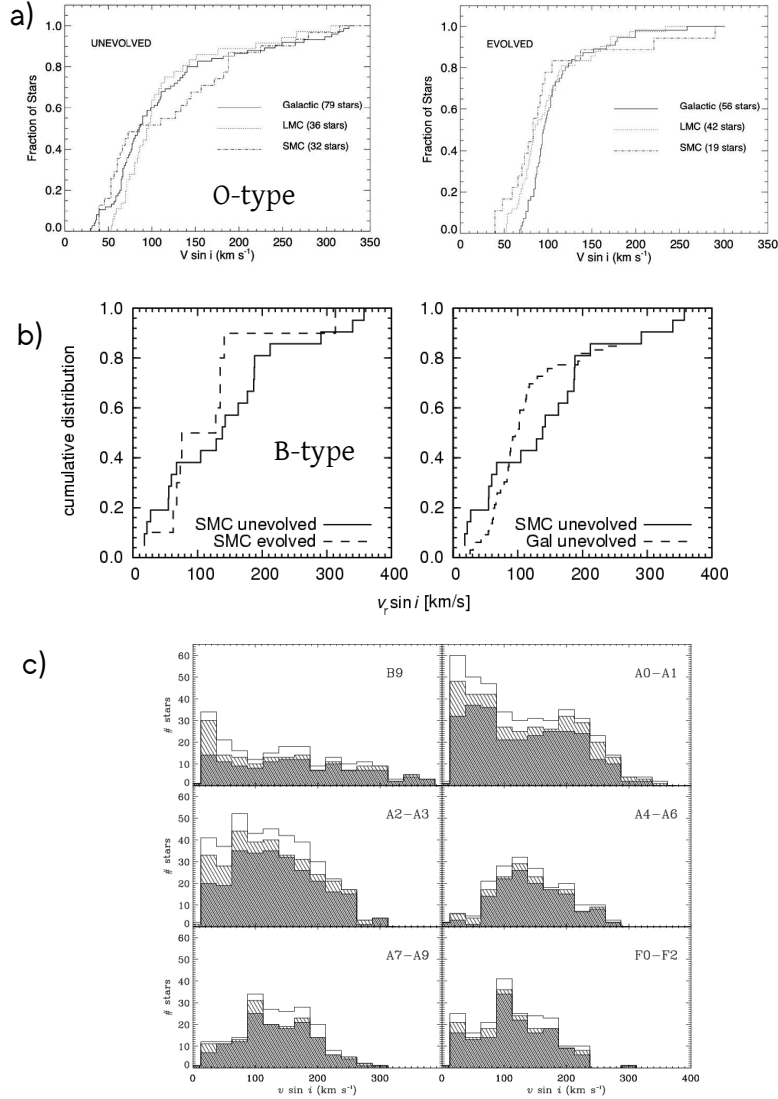


Fig. 1. Rotation of early-type stars. *a)* Projected velocity distribution of O-type stars (From Mokiem et al. 2006); *b)* Projected velocity distribution of B type stars (From Penny & Gies 2009); *c)* Projected velocity distribution for A-type stars (From Royer et al. 2007)

A and F-type stars (Fig. 1c)

A large survey of A and F type stars allowed Royer and collaborators (see Royer et al. 2007 and references therein) to establish a good statistic for their typical rotation. These

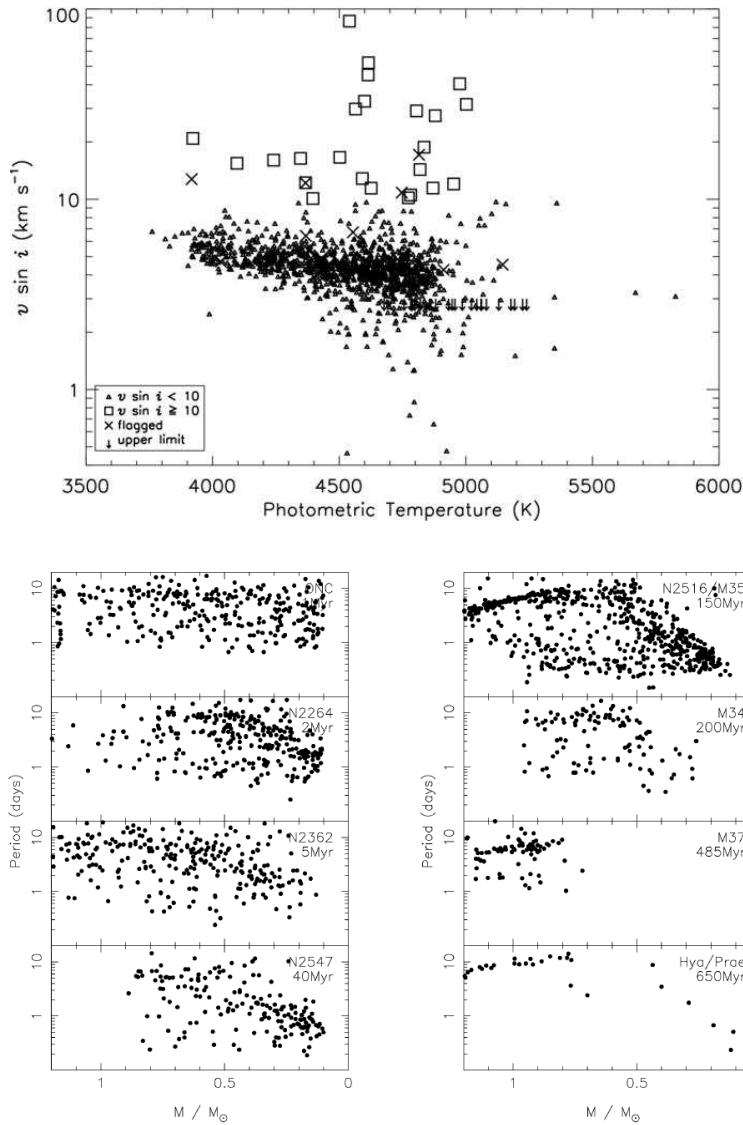


Fig. 2. Rotation of cool stars . Upper panel Projected velocity as a function of surface temperature for a sample of K-type giants (*From Carlberg et al. 2011*); Lower panels Rotation periods as a function of mass and age in a set of open clusters (*From Irwin & Bouvier 2009*).

are generally rapid rotators, $\langle v \sin i \rangle \approx 150 \text{ km.s}^{-1}$, although the velocity distribution is more complex when going into more details for each subtype. For instance, a significant fraction of late A-type stars rotate at more than 50% of their break-up

velocity. Actually part of the fast rotating stars imaged with interferometry and rotating near the break-up limit are A-type stars (see Zhao et al. 2011).

G, K and M-type giants (Fig. 2)

Red giant stars are generally slow rotators, with surface velocities lower than about 10 km.s^{-1} (de Medeiros 2004, Carlberg et al. 2011). However, some of them present unusually higher projected velocities ($\gtrsim 10 \text{ km.s}^{-1}$) as evidenced by Rucinski 1990, Barnbaum et al. 1995, Carlberg et al. 2011, Carlberg et al. 2012. Also evidenced from asteroseismic data, they have been interpreted as the result of some peculiar events that may occur during this phase.

Low-mass pre-main sequence and main sequence stars (Fig. 2)

A large effort has been dedicated to measure rotation periods via photometric surveys of open clusters sampling a wide range of ages (see MONITOR project for instance, and J. Bouvier this volume for more details). These studies show that from an essentially bi-modal distribution of P_{rot} at young ages, the rotation converges to a single low P_{rot} (for solar-type stars) or high P_{rot} (for very low-mass stars - M-type) at the age of the Hyades.

These direct measurements testify the stellar rotation and indicate in some cases as those shown in Fig. 7, that it can lead to significant departures from the spherical symmetry. They also show that the stellar angular velocity (and angular momentum) differs according to spectral type, and thus stellar mass but also time, and that it evolves with time along the stellar life.

Internal rotation of the Sun and of red giants (Fig. 3)

Thanks to helioseismic data from the SoHO satellite (García et al. 2011) and much more recently to the instruments on-board the CoRoT and KEPLER satellites (De Ridder et al. 2009, Beck et al. 2012, Deheuvels et al. 2012, Mosser et al. 2012a, Mosser et al. 2012b), an insight to the *internal rotation profile* of the Sun and of a large number of red giant stars has become available. This opens a completely new road for our understanding of stellar structure and angular momentum distribution and constitutes extremely valuable constraints to stellar models.

Solar-like oscillations are due to the trapping of sound waves excited by convection. Assuming a spherical star, such oscillations appear as a discrete spectrum of degenerate modes characterized by their radial order n and their spherical harmonic degree l . The azimuthal number m is degenerated, a degeneracy that is completely lifted by rotation as well as other aspherical perturbations.

In the Sun, the pressure modes (p -modes) are trapped in relatively superficial cavities and probe the convective envelope and part of the underlying radiative interior, the solar core remaining unprobed. Gravity modes on the other hand (g -modes) are generally confined to inner cavities, and scarcely appear at the surface. They could probe the solar core but do not appear at the solar surface and

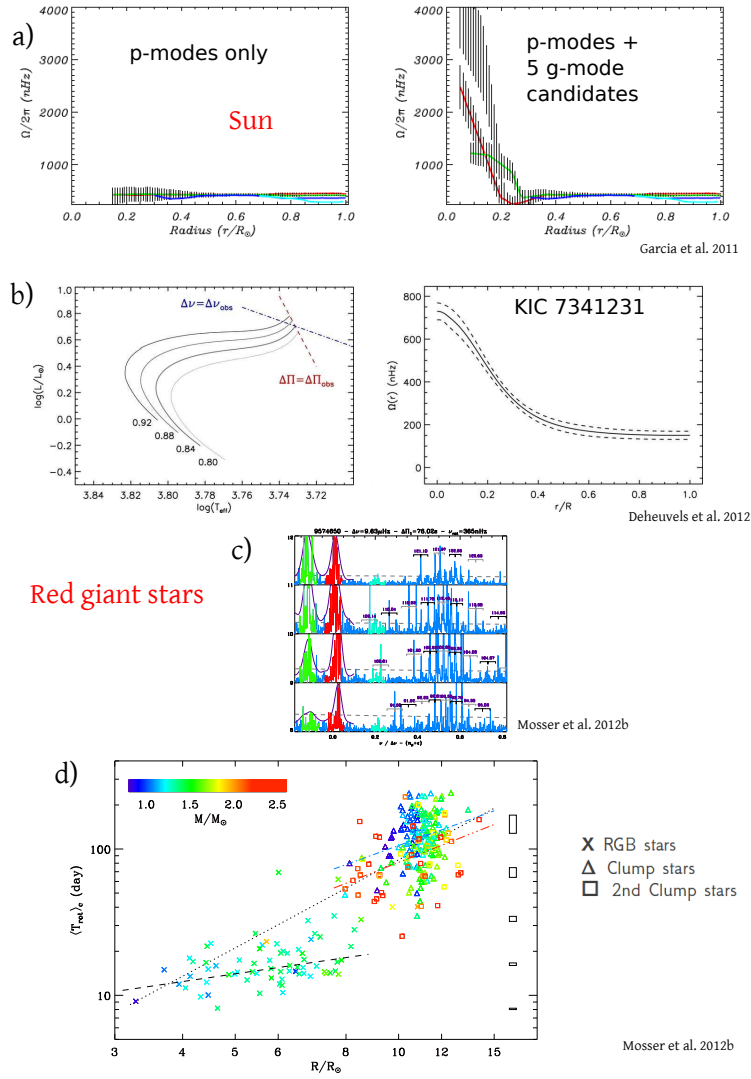


Fig. 3. Probing the internal rotation of stars through solar-like oscillations : *a*) Inversion of the internal rotation profile of the Sun using 4608 days of MDI and GOLF data; *b*) Evolutionary status and internal rotation profile as deduced from mixed-modes for the subgiant KIC 7341231; *c*) Rotational splittings of the mixed modes corresponding to radial orders 8 to 11 in the giant KIC 9574650; *d*) Mean period of core rotation as a function of the asteroseismic stellar radius for about 300 Kepler giants.

are extremely difficult to detect : after 14 years of SoHO data integration, only *g*-mode candidates have been tentatively identified (García et al. 2011). In red giant stars, the situation was discovered to be unexpectedly simpler, since mixed

gravity/pressure modes have been detected. These modes correspond to the coupling of gravity waves in the interior to pressure waves in the envelope and give unprecedented insight on the internal properties of red giant stars.

Figure 3 displays the inverted radial rotation profile of the Sun (García et al. 2011) and of a subgiant in the Kepler field (Deheuvels et al. 2012), as well as a core rotation period - asteroseismic stellar radius plot for a sample of about 300 red giants from the Kepler field (Mosser et al. 2012b). Red giants appear to experience differential rotation in their interior, and hints exist that a similar behaviour could exist in the solar central regions as can be seen from panels a) and b).

Another important point coming out of these data is a clear distinction between clump (e.g. core helium burning stars) and red giant stars (e.g. shell hydrogen burning stars) in terms of core rotation period (panel d)). This provides a new powerful tool to discriminate between stars belonging to these very different evolutionary phases that occupy overlapping regions in the Hertzsprung-Russell diagram and are thus very difficult to distinguish from classical surface parameters as temperature or magnitude.

2.2 Indirect probes of stellar rotation

In addition to the direct measurements, the analysis of the surface chemical properties of stars may constitute a set of evidences for transport processes occurring inside the stars, some of them being attributed to rotation-driven processes.

”Abundance anomalies”, e.g. departures from the predictions of classical¹ stellar evolution models are powerful diagnostic tools to probe the efficiency of transport processes that pollute the stellar atmosphere. Such transport can be of internal origin and connect regions with efficient nucleosynthesis to the surface, or from an external source when material of different chemical composition is accreted onto the star.

As all stars rotate, it is natural to first look for rotation-induced transport processes to explain the discrepancies between abundance observations and predictions of classical and standard stellar evolution models. One should nevertheless bear in mind that a degeneracy exists concerning the nature of the transport processes itself, and that if rotation-driven mechanisms can be found to be dominant in some cases, they are certainly not the only ones acting.

Those abundance variations observed at the surface of stars that reflect nucleosynthetic processes that are known to occur inside these very same stars can be considered as evidences for transport / mixing processes connecting the surface to the regions where the nucleosynthesis occurs. Indeed, the abundances of the products of hydrogen burning via the pp-chains and the *extended* CNO cycle

¹Stellar evolution models including no transport of matter in the radiative regions are referred to as *classical* models. The only *mixed* regions are convectively unstable ones. *Standard* stellar evolution models account for microscopic diffusion processes that may occur on long time scales in radiative regions such as gravitational settling or radiative levitation.

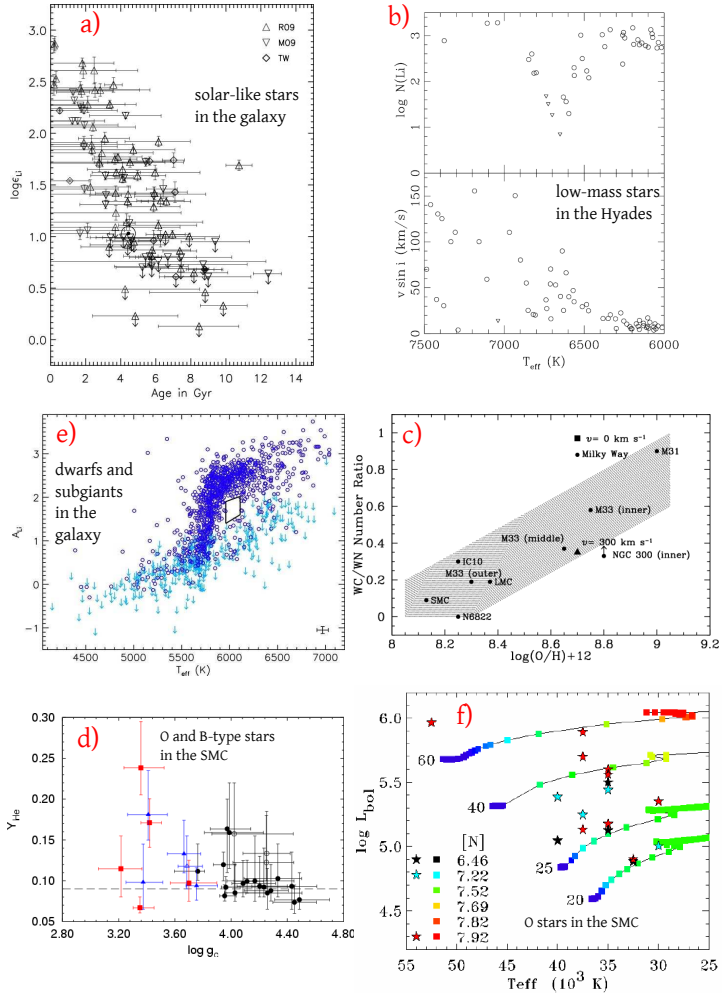


Fig. 4. **a** Lithium abundances in solar-type stars as a function of age (from Baumann et al. 2010); **b** Lithium abundances and projected rotation velocities as a function of T_{eff} in stars of the Hyades (from Talon & Charbonnel 1998); **c** Number population of two types of Wolf-Rayet stars as a function of metallicity traced by the oxygen abundance (from Meynet & Maeder 2003); **d** He overabundances in O-type stars of the Magellanic Clouds (from Mokiem et al. 2006); **e** Li abundances as a function of T_{eff} for a sample of dwarfs and subgiants in the Galaxy (from Mishenina et al. 2012); **f** Nitrogen abundances in O-type stars of the SMC (from Heap et al. 2006)

(including NeNa- and MgAl- chains) can be used to trace internal mixing when variations are observed at evolutionary phases where they are not expected from

standard stellar evolution models. In red giant stars, the presence of *s*-process² at the surface may also be considered as evidence for internal mixing. Figure 4 presents a set of observed abundance patterns that are used as indirect probes for internal (rotational) mixing:

- Lithium depletion during phases where no convective dredge-up is expected → in low- and intermediate-mass stars (Boesgaard 1989, Boesgaard & Tripicco 1986, Gratton et al. 2000, Baumann et al. 2010, Canto Martins et al. 2011, Mishenina et al. 2012)
- Lithium enrichment → in low- and intermediate-mass stars (Charbonnel & Balachandran 2000, Lèbre et al. 2009)
- Boron and Beryllium depletion → in low-, intermediate-mass, and massive stars (Boesgaard 2005, Boesgaard et al. 2005a, Boesgaard & Krugler Hollek 2009)
- Carbon depletion and carbon isotopic ratio decrease → in low-mass red giant stars, in main sequence and post main sequence massive stars (Gratton et al. 2000)
- Nitrogen enrichment → in low-mass red giant stars, in main sequence and post main sequence massive stars (Frebel et al. 2005, Heap et al. 2006, Martins et al. 2009)
- Helium enrichment → in massive O-type stars at low metallicity (Mokiem et al. 2006)
- *s*-process elements enrichment → in intermediate-mass AGB stars

The fact that abundance anomalies increase with decreasing metallicity may also be viewed as an evidence for rotation-driven transport inside the stars, as some of these mechanisms are expected to be more efficient as stars become more compact and bluer at low metallicity.

Population counts, in particular for the subtypes of massive stars at different evolutionary phases (subtypes of supergiants, of Wolf-Rayet and O and B type stars) can also be used as indirect probes of internal mixing (Eggenberger et al. 2002, Meynet & Maeder 2003, Martins et al. 2009).

Figure 4 presents a set of observed abundance patterns that are used as indirect probes for internal (rotational) mixing.

In § 6 we will show how stellar evolution models of rotating stars confront to direct and indirect probes.

²The *s*-process is a nucleosynthesis path that involves the production of heavy elements by slow neutron captures (Clayton 1984).

3 Modelling the structural evolution of rotating stars

It appears from observations that rotation may actually modify the shape of stars, their lifetimes, their surface parameters and abundances. These evidences constitute a strong incitement to actually include rotation and associated physical processes in stellar evolution modelling.

In this section, I present the different approaches, prescriptions and techniques that are used in stellar evolution codes to account for the direct effects of rotation on the stellar structure and evolution, leaving rotation-induced transport of angular momentum and nuclides for § 4.

3.1 Stellar Structure Equations : standard formulation

A star is a continuous plasma that should be described by fully tri-dimensional hydrodynamical equations :

$$\text{Continuity equation} \quad \frac{\partial \rho}{\partial t} = -\vec{\nabla} \cdot (\rho \vec{v}) \quad (3.1)$$

$$\text{Motion equation} \quad \rho \frac{d\vec{v}}{dt} = -\vec{\nabla} P - \rho \vec{\nabla} \Phi \quad (3.2)$$

$$\text{Energy conservation equation} \quad T \frac{d\rho s}{dt} = \rho \epsilon_{prod} - \vec{\nabla} \cdot \vec{F} \quad (3.3)$$

$$\text{Heat transfer equation} \quad \vec{F} = -\mathcal{K} \vec{\nabla} T \quad (3.4)$$

$$\text{Abundance conservation equation} \quad \frac{\partial n_i}{\partial t} + \vec{\nabla} \cdot n_i \vec{v}_i = - \sum_j \mathcal{R}_{ij} n_i n_j + \sum_{k,l} \mathcal{R}_{kl} n_k n_l \quad (3.5)$$

where ρ is the density; \vec{v} is the macroscopic velocity; P is the total pressure (given by the equation of state); Φ is the gravitational potential derived from the Poisson equation $\nabla^2 \Phi = 4\pi G \rho$; s is the specific entropy (defined by the second principle of thermodynamics); T is the local temperature; ϵ_{prod} is the energy production rate par unit mass and time; \vec{F} is the heat flux; \mathcal{K} is the thermal conductivity tensor; n_i is the volumetric abundance of chemical species i ; \vec{v}_i is the microscopic velocity of particles of species i ; \mathcal{R}_{kl} is the rate of destruction (if k or l are equal to i) or production of species i by unit volume and time for a particle of species i .

When studying a non-rotating, weakly or non-magnetic single star, pressure and gravity are the only forces acting on a mass element. The resulting spherically symmetric configuration allows to reduce the problem of stellar evolution to the resolution of a set of equations that only depend on time and one spatial coordinate.

Instead of the natural eulerian formulation that would derive from expressing the above listed equations as a function of the radius r only, the Lagrangian formulation is normally preferred. The spatial coordinate is now the mass m associated to a radius r and the resulting set of stellar structure equations is the following:

$$\frac{\partial r}{\partial m} = \frac{1}{4\pi r^2 \rho} \quad (3.6)$$

$$\frac{\partial P}{\partial m} = -\frac{1}{4\pi r^2} \left(\frac{Dv}{Dt} + \frac{\partial \Phi}{\partial m} \right) = -\frac{1}{4\pi r^2} \left(\frac{Dv}{Dt} + \frac{Gm}{r^2} \right) \quad (3.7)$$

$$\frac{\partial L}{\partial m} = \epsilon_n - \epsilon_\nu - C_p \frac{\partial T}{\partial t} + \frac{\delta}{\rho} \frac{\partial P}{\partial t} = \epsilon_n - \epsilon_\nu + \epsilon_g \quad (3.8)$$

$$\frac{\partial T}{\partial m} = -\frac{GmT}{4\pi r^4 P} \frac{d \ln T}{d \ln P} \Big|_{\text{medium}} = -\frac{GmT}{4\pi r^4 P} \nabla \quad (3.9)$$

$$\frac{\partial X_i}{\partial t} = \frac{m_i}{\rho} \left(\sum_j r_{ji} - \sum_k r_{ik} \right) \quad \forall i \quad (3.10)$$

$$L = 4\pi r^2 (F_{conv} + F_{rad}) = \frac{16\pi acGmT^4}{3\kappa P} \nabla_{rad} \quad (3.11)$$

where $\frac{Dv}{Dt} \Big|_m$ is the Lagrangian derivative equal to $\frac{\partial v}{\partial t} + v \frac{\partial v}{\partial r}$; ϵ_n , ϵ_ν and ϵ_g are the nuclear, neutrino, and gravitational energies resp.; $\delta = \left(\frac{d \ln \rho}{d \ln T} \right)_P$ entering the equation of state (Kippenhahn & Weigert 1990); X_i is the mass fraction of nuclide i ; m_i is the mass of nuclide i ; r_{ji} is the rate for the nuclear reaction between nuclide j and i ; $a = \frac{4\sigma}{3} = 7.5657 \times 10^{-15} \text{ erg.cm}^{-3}.\text{K}^{-4}$ is the radiation constant and $\sigma = 5.6704 \times 10^{-8} \text{ erg.cm}^{-2}.\text{s}^{-1}.\text{K}^{-4}$ is the Stefan's constant.

These equations need to be complemented by (1) an equation of state $\rho = \rho(P, T, \mu)$, (2) an expression for the mean Rosseland opacity of the plasma, $\kappa = \kappa(P, T, \mu)$ (in most stellar evolution codes, opacities are tabulated), (3) a network of nuclear reactions rates r_{ij} , (4) an equation for energy production/losses by neutrinos ϵ_ν and (5) a description of the energy transport by convection to obtain \vec{F}_{conv} .

The convective flux, hence the temperature gradient ∇ , is generally derived from the mixing length theory (Böhm-Vitense 1958). The formulation by Kippenhahn & Weigert (1970) gives:

$$F_{conv} = \rho C_p T \sqrt{g \delta} \frac{l^2}{4\sqrt{2}} H_p^{-3/2} (\nabla - \nabla_e)^{1/2} \quad (3.12)$$

where $H_p = -\frac{dr}{d \ln P}$ is the pressure scale height. $l = \alpha_{MLT} H_p$ is the so-called “*mixing length*” over which a fluid element dissolves completely into its surroundings, with α_{MLT} a parameter of order unity that is calibrated by having a $1 M_\odot$ model reproducing the Sun's radius, luminosity and temperature at the age of the Sun. $\nabla_e = \frac{d \ln T}{d \ln P} \Big|_e$ is the temperature gradient of the fluid element.

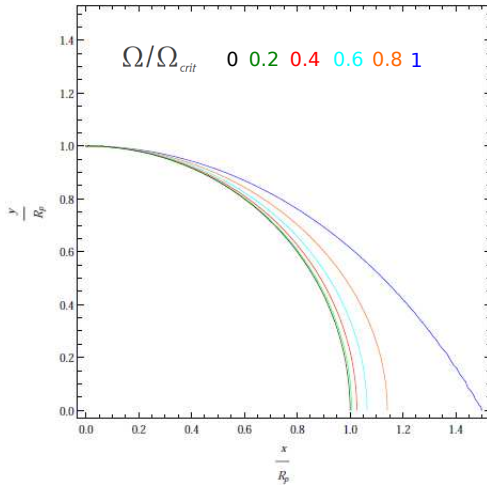


Fig. 5. Distortion of a rotating star with the Roche model. Each color corresponds to the mentioned values of the ratio $\omega = \Omega/\Omega_{\text{crit}}$ with $\Omega_{\text{crit}} = \sqrt{\frac{8GM}{27R_p^3}}$, M the stellar mass, Ω the angular velocity at the surface and R_p the polar radius. *Courtesy A. T. Potter (Potter 2012).*

3.2 Stellar Structure Equations : the case of rotating stars

The mechanical equilibrium of a star is modified when rotation is taken into account, because the rotating star is not spherical any more. This departure from spherical symmetry translates into

- the deformation of the equipotential surfaces;
- the reduction of the effective gravity away from the rotation axis by centrifugal forces;
- the variation of the radiative flux on equipotential surfaces (Von Zeipel effect).

This list reveals immediately that rotation calls for a multi-dimensional description of the stellar structure. However, this is a real challenge for stellar evolution modelling, stellar evolution being meant here as the *integration of all evolutionary phases from birth to final stages*. The difficulty arises from the huge variety of spatial and temporal scales involved (about 10^{11} and 10^{17} orders of magnitude for spatial and temporal scales respectively for solar-type star if microscopic processes and convection are to be treated properly).

Although great efforts are devoted to move from the 1D picture to a 2D (see also Rieutord this volume, and Rieutord & Espinosa Lara 2013) or 3D modelling (Turcotte et al. 2003, Bazan et al. 2003), the stellar evolution models presently in use to interpret most of observations are the result of 1D modelling

3.2.1 The Roche model for distorted rotating stars

Two families of historical approaches exist to evaluate the shape of a rotating fluid : The *MacLaurin's spheroids*, which assume that the rotating fluid, e.g. the

star, is a body of constant density and uniform angular velocity, and the *Roche equipotentials* which assume that the gravitational potential Φ is the same as if the total mass of the star were concentrated at the centre.

In each of these families, the total potential writes as the sum of the gravitational potential and of the potential from which the centrifugal acceleration derives when the star is *barotropic*.

Although none of these visions are correct, the Roche model is much more appropriated to model a star and is very commonly used.

For a barotropic star, the centrifugal acceleration derives from a potential V

$$V = -\frac{1}{2}s^2\Omega^2 \quad (3.13)$$

with s the distance from the rotation axis, and Ω the angular velocity. On the other hand, the gravitational potential is defined by

$$-\vec{\nabla}\Phi = -\frac{Gm}{r^2}\frac{\vec{r}}{r},$$

and is spherically symmetric in the Roche approximation so that

$$\Phi = -\frac{Gm}{r}. \quad (3.14)$$

Here G is the gravitational constant and m is the mass inside the sphere of radius r .

In the Roche approximation, the total potential thus writes

$$\Psi(r, \theta) = \Phi + V = -\frac{Gm}{r} - \frac{1}{2}\Omega^2 r^2 \sin^2 \theta. \quad (3.15)$$

The stellar surface is an equipotential, $\Psi = \text{const}$. As the centrifugal force vanishes at the poles, the following equation can thus be used to define the stellar surface :

$$\frac{GM}{R} + \frac{1}{2}\Omega^2 R^2 \sin^2 \theta = \text{const} = \frac{GM}{R_p}, \quad (3.16)$$

where M and R are the total mass and radius of the star, and R_p is the polar radius. Its critical value, obtained where the gravity exactly compensates the centrifugal acceleration in the equatorial plane is :

$$\Omega_{P,\text{crit}} = \sqrt{\frac{8GM}{27R_{P,\text{crit}}^3}} \quad (3.17)$$

Figure 5 represents the stellar surface in reduced radius units for different rotation rates as indicated on the graph. We can see that up to $\omega \approx 0.6$, the equatorial radius increase is lower than 10%, and only for the very rapid rotators should we expect a strong distortion. This remark is important as it justifies a perturbative approach to model the evolution of most rotating stars.

3.2.2 Kippenhahn & Thomas (1970): Case of conservative rotation law

Noticing that pressure P and density ρ are constant on equipotentials if the potential is conservative, Kippenhahn & Thomas (1970) propose to re-write the stellar structure equations on these equipotentials, that can be distorted and thus account for the spherical symmetry departure induced by rotation.

So let's Ψ be a conservative potential, and equipotentials be defined as surfaces where $\Psi = \text{const}$. For the potential to be conservative, it means that the centrifugal acceleration derives from a potential.

In Kippenhahn & Thomas (1970), Ψ is the Roche potential from Eq. (3.15).

In Endal & Sofia (1976), the potential is a Kopal-type potential (Kopal 1959), divided in three parts,

$$\Psi = \Psi_s + \Psi_r + \Psi_d \quad (3.18)$$

with Ψ_s , the spherically symmetric part of the gravitational potential, Ψ_r , the cylindrically symmetric potential directly due to rotation and Ψ_d the cylindrically symmetric part of the gravitational potential due to the distortion of the star's shape :

$$\Psi_s = -\frac{Gm}{r} \quad (3.19)$$

$$\Psi_r = \frac{1}{2}r^2 \sin^2 \theta \Omega^2 \quad (3.20)$$

$$\Psi_d = \sum_{j=2}^{\infty} \frac{4\pi G}{(2j+1)r^{j+1}} \int_0^{r_0} \rho \frac{\partial}{\partial r'_0} (r_0'^{j+3} Y_j) dr'_0 \quad (3.21)$$

where r_0 is the radius of the equipotential with angle θ_0 so that $P_2(\cos \theta_0) = 0$, with P_2 the second order Legendre polynomial and Y_j is the axisymmetric tesseral harmonic relating r to r_0 on an equipotential (see Appendix A in Endal & Sofia 1976 for further details).

For a conservative potential, we can define a mean radius for the equipotential, r_Ψ as the radius of the sphere containing the same volume V_ψ as the equipotential of surface S_Ψ

$$V_\Psi = \frac{4}{3}\pi r_\Psi^3 \quad (3.22)$$

This expression preserves the form of the continuity equation, where r and m are replaced by r_Ψ and m_Ψ .

The mean of any physical quantity u that is not constant on the equipotential surfaces can be written as

$$\langle u \rangle = \frac{1}{S_\Psi} \int_{\Psi=\text{const}} u dS_\Psi. \quad (3.23)$$

The gravity derives from the total potential, that is

$$\vec{g} = -\vec{\nabla}\Psi \longrightarrow g = \frac{d\Psi}{dn} \quad (3.24)$$

with dn the distance between equipotentials $\Psi = \text{cst}$ and $\Psi + d\Psi = \text{cst}$. It is not constant over the equipotential surfaces, yielding :

$$\langle g \rangle = \frac{1}{S_\Psi} \int_{\Psi=\text{cst}} \frac{d\Psi}{dn} dS_\Psi \quad \text{and} \quad \langle g^{-1} \rangle = \frac{1}{S_\Psi} \int_{\Psi=\text{cst}} \left(\frac{d\Psi}{dn} \right)^{-1} dS_\Psi. \quad (3.25)$$

We can also define a volume element $dV_\Psi = d\Psi \int_{\Psi=\text{cst}} \left(\frac{dn}{d\Psi} \right) dS_\Psi$, and thus relate the potential derivative to the density and the mean of the inverse gravity:

$$d\Psi = \frac{1}{S_\Psi \langle g^{-1} \rangle} \frac{dm_\Psi}{\rho}. \quad (3.26)$$

The modification of the stellar structure equations is then straightforward from Eqs. (3.22) and (3.26). As an example, the hydrostatic equilibrium (Eq. 3.7 with $v = 0$) becomes :

$$\begin{aligned} \vec{\nabla} P &= -\rho \vec{\nabla} \Psi \\ \frac{\partial P}{\partial m_\Psi} &= -\rho \frac{\partial \Psi}{\partial m_\Psi} = -\rho \frac{Gm_\Psi}{r_\Psi^2} \frac{1}{4\pi r_\Psi^2 \rho} \\ \frac{\partial P}{\partial m_\Psi} &= -\frac{Gm_\Psi}{4\pi r_\Psi^4} f_P \end{aligned} \quad (3.27)$$

with

$$f_P = \frac{4\pi r_\Psi^4}{Gm_\Psi S_\Psi} \frac{1}{\langle g^{-1} \rangle} \quad (3.28)$$

The complete new set of stellar structure equations ³ finally writes:

$$\frac{\partial r_\Psi}{\partial m_\Psi} = \frac{1}{4\pi r_\Psi^2 \rho} \quad (3.29)$$

$$\frac{\partial P}{\partial m_\Psi} = -\frac{Gm_\Psi}{4\pi r_\Psi^4} f_P \quad (3.30)$$

$$\frac{\partial L_\Psi}{\partial m_\Psi} = \epsilon_n - \epsilon_\nu + \epsilon_g \quad (3.31)$$

$$\frac{\partial T}{\partial m_\Psi} = -\frac{Gm_\Psi T}{4\pi r_\Psi^4 P} \nabla_\Psi \quad (3.32)$$

$$L_\Psi = -\frac{4acT^3}{3\kappa} \langle g^{-1} \rangle S_\Psi^2 \langle g \rangle \frac{\partial T}{\partial m_\Psi} \quad (3.33)$$

with

$$\nabla_\Psi = -\frac{3\kappa}{16\pi acG} \frac{P}{T^4} \frac{L_\Psi}{m_\Psi} \frac{f_T}{f_P} \quad (3.34)$$

³We omit here the abundance conservation equation that can be written as in Eq. (3.10).

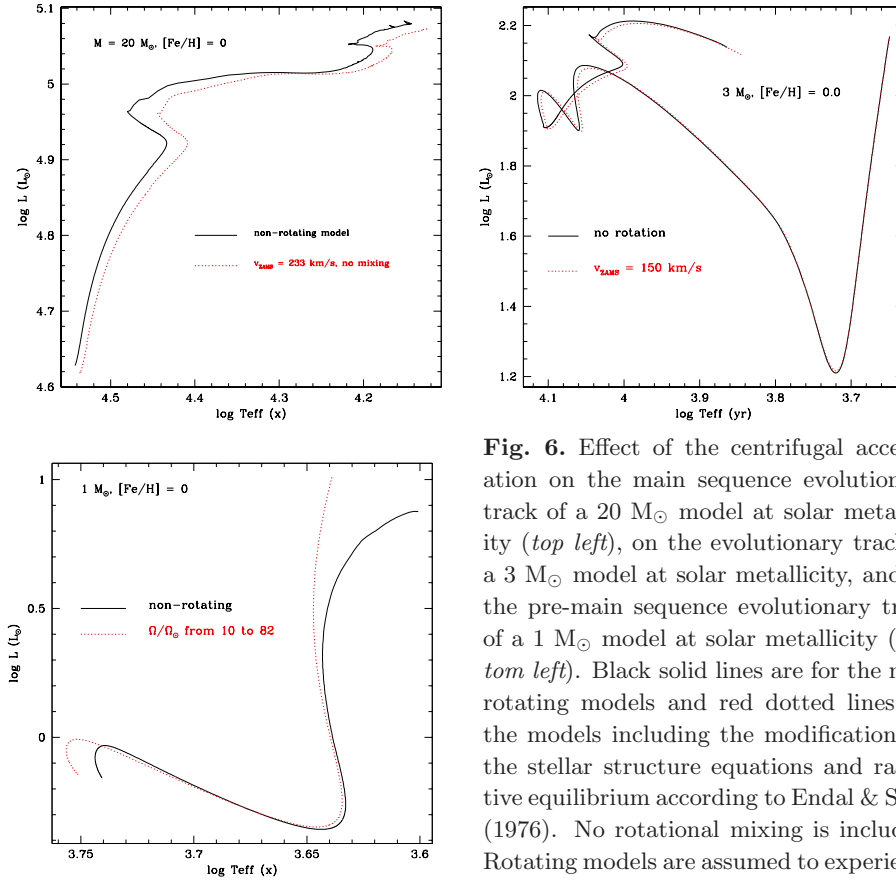


Fig. 6. Effect of the centrifugal acceleration on the main sequence evolutionary track of a $20 M_{\odot}$ model at solar metallicity (*top left*), on the evolutionary track of a $3 M_{\odot}$ model at solar metallicity, and on the pre-main sequence evolutionary track of a $1 M_{\odot}$ model at solar metallicity (*bottom left*). Black solid lines are for the non-rotating models and red dotted lines for the models including the modifications of the stellar structure equations and radiative equilibrium according to Endal & Sofia (1976). No rotational mixing is included. Rotating models are assumed to experience solid-body rotation.

and

$$f_T = \left(\frac{4\pi r_{\Psi}^2}{S_{\Psi}} \right)^2 \frac{1}{\langle g \rangle \langle g^{-1} \rangle}. \quad (3.35)$$

This set of equations is very similar to the standard set of stellar structure equations, with the addition of *deformation* factors f_P and f_T to the motion and heat transfer (radiative equilibrium through the gradient ∇_{Ψ}) equations.

Figure 6 shows the impact of the centrifugal acceleration on the evolutionary track of a main sequence massive ($20 M_{\odot}$) star, of an intermediate-mass star ($3 M_{\odot}$) from the pre-main sequence (hereafter PMS) to the subgiant phase, and of a PMS low-mass star ($1 M_{\odot}$).

Centrifugal acceleration lowers effective gravity, which in turn translates into a

decrease of both the luminosity and the effective temperature. Including the centrifugal force in the total potential of the star makes it behave as if it were a non rotating, slightly less massive star. This effect is the same for the different masses and evolutionary stages presented on the figure (see also Pinsonneault et al. 1989, Martin & Claret 1996, Mendes 1999, Eggenberger et al. 2010, Eggenberger et al. 2012). As we will show later, the hydrostatic effects constitute the main effect of rotation on the evolutionary tracks of low- and intermediate-mass stars beyond the turn-off.

3.2.3 Meynet & Maeder (1997): Case of non-conservative rotation law

The formalism developed by Kippenhahn & Thomas (1970) is only valid for conservative rotation and needs to be revised for non-conservative rotation laws. Among those, the *shellular rotation* introduced by Zahn 1992 (see also Chaboyer & Zahn 1992) provides the first self-consistent formalism for the transport of angular momentum by meridional circulation and shear turbulence (see § 5).

Shellular rotation is expected to occur in radiative stellar interiors, where turbulence develops (because the plasma is highly inviscid) and where it is supposed to be highly anisotropic. Horizontal turbulent motions are presumably more vigorous than vertical ones, and provided this anisotropy is large ($\nu_v \ll \nu_h$), the angular velocity profile depends very weakly on colatitude, so that $\Omega \equiv \Omega(r)$.

Such rotation law is non-conservative and the centrifugal acceleration does not derive from a potential any more. Meynet & Maeder (1997) present an extension of Kippenhahn & Thomas (1970) formalism to integrate this fact.

The main difference between conservative and non-conservative rotation laws is the following :

- in the case of solid-body rotation, $\Omega = cst$, which is a conservative law, the isobars coincide with the equipotential surfaces, and the star is **barotropic**. The equations of the stellar structure can then be projected on equipotentials;
- in the case of shellular rotation, $\Omega = \Omega(r)$, which is a non-conservative law, the isobars do not coincide with the equipotentials nor with isotherms (they are inclined with respect to the horizontality defined by the equipotentials), and the star is **baroclinic**. The equations of the stellar structure are then better projected on the *isobars*. On these surfaces Ω is constant.

The approach of Meynet & Maeder (1997) is to use a formalism similar to that of Kippenhahn & Thomas (1970), replacing the equipotentials by the isobars. These surface have the same shape as the equipotential in the conservative case. They are defined as surfaces where Ψ_P is constant with

$$\Psi_P = -\Phi + \frac{1}{2}\Omega^2 r^2 \sin^2 \theta \quad (3.36)$$

and Φ the gravitational potential in its Roche form, r the radius and θ the colatitude.

The subscripts Ψ in Eqs. (3.29) to (3.32) are thus replaced by a subscript P , and provided some reasonable assumptions⁴, they finally obtain the following set of equations:

$$\frac{\partial r_P}{\partial m_P} = \frac{1}{4\pi r_P^2 \bar{\rho}} \quad (3.37)$$

$$\frac{\partial P}{\partial m_P} = -\frac{Gm_P}{4\pi r_P^4} f_P \quad (3.38)$$

$$\frac{\partial L_P}{\partial m_P} = \epsilon_n - \epsilon_\nu + \epsilon_g \quad (3.39)$$

$$\frac{\partial T}{\partial m_P} = -\frac{Gm_P T}{4\pi r_P^4 P} \nabla_P \quad (3.40)$$

$$L_P = -\frac{4ac}{3} \langle g_{\text{eff}}^{-1} \rangle S_P^2 \left\langle \frac{T^3 g}{\kappa} \right\rangle \frac{\partial T}{\partial m_P} \quad (3.41)$$

with

$$\nabla_P = -\frac{3\kappa}{16\pi acG} \frac{P}{T^4} \frac{L_P}{m_P} \frac{f_T}{f_P} \quad (3.42)$$

and

$$f_P = \frac{4\pi r_P^4}{Gm_P S_P} \frac{1}{\langle g^{-1} \rangle}. \quad (3.43)$$

$$f_T = \left(\frac{4\pi r_P^2}{S_P} \right)^2 \frac{1}{\langle g \rangle \langle g^{-1} \rangle}. \quad (3.44)$$

The effective gravity, noted g for sake of simplicity, also has a different expression. It depends on the radius r and on the colatitude θ :

$$\vec{g} \equiv \vec{g}_{\text{eff}} = \vec{\nabla} \Psi_P - r^2 \sin^2 \theta \Omega \vec{\nabla} \Omega.$$

It cannot be expressed as the derivative of Ψ_P , since this quantity is not a potential in the baroclinic case. From the hydrostatic equilibrium equation

$$\vec{P} = -\rho \left(\vec{\nabla} \Psi_P - r^2 \sin^2 \theta \Omega \vec{\nabla} \Omega \right)$$

and noticing that $\vec{\nabla} \Omega$ is parallel to $\vec{\nabla} \Psi_P$, an expression for g_{eff} can be given by

$$g \equiv g_{\text{eff}} = (1 - r^2 \sin^2 \theta \Omega \alpha) \frac{d\Psi_P}{dn} \quad (3.45)$$

⁴see Equations (A.23) to (A.26) in Meynet & Maeder (1997)

where $\alpha = \frac{d\Omega}{d\Psi_P}$.

The set of equations of § 3.2.2 is actually recovered if one assumes that all quantities do not depend on the local density and temperature, but on their volume averaged means between two isobars, $\bar{\rho}$ and \bar{T} , with

$$\bar{\rho} = \frac{\rho (1 - r^2 \sin^2 \theta \Omega \alpha) \langle g^{-1} \rangle}{\langle g^{-1} \rangle - \langle g^{-1} r^2 \sin^2 \theta \rangle \Omega \alpha}. \quad (3.46)$$

Zeng (2002) proposed a complete generalization of this formalism to the case of unspecified rotation law. The projection of the general set of equations for stellar structure is done on isobars again, but tunable parameters (4) are added which somehow weakens the approach.

3.3 Radiative transfer : the case of rotating stars

3.3.1 Gravity darkening

The radiative flux of a star writes as

$$\vec{F} = -\frac{4ac}{3\kappa\rho} T^3 \vec{\nabla} T = \frac{4ac}{3\kappa\rho} T^3 \frac{dT}{d\Psi} \vec{\nabla} \Psi. \quad (3.47)$$

When the star is rotating, the total potential Ψ depends on the angular velocity Ω and on the colatitude θ . Its gradient is not constant on an equipotential because the spacing between equipotentials decreases when moving from the equator to the polar regions. It follows that $\vec{\nabla} \cdot \vec{F} = f((\nabla\Psi)^2) = 0$ cannot be verified at all colatitudes and the radiative equilibrium is broken.

The Von Zeipel theorem, established in 1924 (von Zeipel 1924) gives the relation between the radiative flux and the local effective gravity. For solid-body rotation, the hydrostatic equilibrium leads

$$\vec{F} = A \vec{\nabla} T = A \frac{dT}{dP} \vec{\nabla} P \underset{\text{hydro.equ.}}{=} -\rho A \frac{dT}{dP} \vec{g} \quad (3.48)$$

where $A = \frac{4act^3}{3\kappa\rho}$ and T, F, P and g_{eff} depend on Ω and on the colatitude θ .

In parallel the total luminosity on an equipotential surface S_P is by definition the integral of the flux on that surface :

$$L = \iint_{S_\Psi} \vec{F} \cdot \vec{n} dS_\Psi \underset{\text{solid.rot.}}{=} \rho A \frac{dT}{dP} \iint_{S_\Psi} \vec{\nabla} \Psi \cdot \vec{n} dS_\Psi \quad (3.49)$$

Using the Poisson equation $\Delta\Psi = 4\pi G\rho - 2\Omega^2$, we can express the luminosity as a function of the density and the angular velocity:

$$L = \rho A \frac{dT}{dP} \iiint_{V_\Psi} (4\pi G\rho - 2\Omega^2) dV_\Psi \quad (3.50)$$

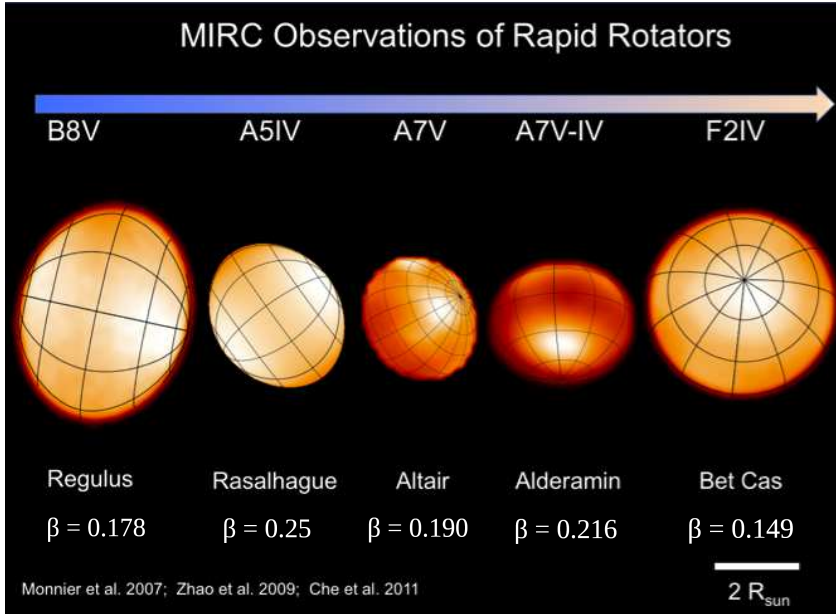


Fig. 7. CHARA/MIRC imaging of 6 rapid rotators, spanning a wide spectral range from B8 to F2 spectral types. The stars are scaled relatively to their linear sizes. The stars are oblate due to their rapid rotation. The polar areas of these stars are bright and their equatorial areas are dark because of the gravity darkening effect. The β exponent for the best-fit models from Zhao et al. (2011) is also indicated. *Adapted from M. Zhao, public comm.*

Putting back the result of the integral in Eq. (3.48), one finally finds

$$\vec{F} = \frac{L}{4\pi GM_\star} \vec{g} \quad (3.51)$$

where $M_\star = M \left(1 - \frac{\Omega^2}{2\pi G \rho_m}\right)$.

The so-called *gravity-darkening effect* directly results from this relation that implies a new relation between effective temperature and gravity

$$T_{\text{eff}} = \frac{L}{4\pi GM_\star} g^{1/4}. \quad (3.52)$$

As the effective gravity $g \equiv g_{\text{eff}}$ is lower at the equator due to the centrifugal force, the poles of a rotating star should be hotter than the equatorial regions. This effect is called *gravity darkening*.

This derivation assumes solid-body rotation, and thus corresponds to a *barotropic star*. For a *baroclinic star*, as is the case when $\Omega = \Omega(r)$, the expression is slightly

modified as demonstrated by Maeder (1999); the radiative flux then depends on the effective gravity and on the gradient of the angular velocity $d\Omega/dr$.

The Von Zeipel theorem concerns the radiative flux, so that the relation $T_{\text{eff}} \propto g_{\text{eff}}^\beta$, with $\beta = 0.25$ should be only valid for stars with radiative envelopes (stars of type A and earlier). A similar relation was established by Lucy (1967) for stars with a convective envelope and yields

$$T_{\text{eff}} \propto g_{\text{eff}}^{0.08}. \quad (3.53)$$

The gravity-darkening has actually been directly observed by NIR interferometric imaging as shown in Fig. 7 (see also Zhao et al. 2011 and references therein for a recent review on the interferometric studies of rapid rotators). However, Eq. (3.52) appears to give a bad fit to the data and overestimates the difference between the polar and equatorial temperature. Based on the presumed variation of the β exponent from 0.25 for radiative envelopes to 0.08 for convective envelopes, a general expression in the form

$$T_{\text{eff}} \propto g_{\text{eff}}^\beta$$

is generally used, with β an adjustable parameter varying between 0.1 and 0.25.

Very recently, Espinosa Lara & Rieutord (2011) have proposed another expression for the gravity-darkening effect which is more suited for fast rotators stars targeted by interferometric imaging⁵:

$$\vec{F} = -\frac{L}{4\pi Gm} F_\omega(r, \theta) \vec{g}_{\text{eff}}, \quad (3.54)$$

where r and θ are the radial and latitudinal coordinates at the stellar surface in spherical geometry, and $F_\omega(r, \theta)$ is a non-dimensional function that is determined within the framework of the Roche model for the mass distribution. $\omega = \sqrt{\Omega^2 R_e^3 / GM}$ is the only parameter controlling the latitudinal variation of the effective temperature, and it is defined as the ratio of the angular velocity to the keplerian velocity at the equator $\Omega_k = \sqrt{g_e / R_e}$.

3.3.2 Mass loss of massive and luminous rapid rotators

Let us summarize here the work by Maeder & Meynet (2000a) concerning the effect of rotation on radiative equilibrium of luminous massive stars and on mass loss.

In massive early-type stars, the radiative flux is important and needs to be taken into account to define the total gravity, which is written:

$$\vec{g}_{\text{tot}} = \vec{g}_{\text{eff}} + \vec{g}_{\text{rad}} \quad (3.55)$$

⁵Von Zeipel's and Lucy's expressions are derived implicitly assuming a small deviation from the spherical symmetry, which should not be the case for very rapid rotators.

where g_{eff} is the sum of the gravitational and centrifugal accelerations and g_{rad} is the radiative acceleration. Both the centrifugal and the radiative accelerations counteract the gravity, and may yield to the break-up limit, when $\vec{g}_{\text{tot}} = \vec{0}$.

One can define the Eddington limit or Γ limit as the break-up limit when rotation is negligible, e.g. when $\vec{g}_{\text{grav}} + \vec{g}_{\text{rad}} = \vec{0}$.

If rotation (e.g. centrifugal acceleration) is important, this Γ limit becomes what Maeder & Meynet (2000a) call the $\Omega\Gamma$ limit defined by $\vec{g}_{\text{tot}} = \vec{0}$.

As mentioned before, for a *baroclinic* rotating star ($\Omega = \Omega(r)$), the von Zeipel theorem is slightly modified to account for baroclinicity:

$$\vec{F} = -\frac{L(P)}{4\pi GM_\star} \underbrace{\vec{g}_{\text{eff}} (1 + \zeta(\theta))}_{\text{baroclinicity}} \quad (3.56)$$

$$\text{where } \zeta(\theta) = \left[\left(1 - \frac{\chi_T}{\delta}\right) \Theta + \frac{H_T}{\delta} \frac{d\Theta}{dr} \right] P_2(\cos \theta).$$

M_\star is the same as in Eq. (3.52), δ is defined by the equation of state (see § 3.1), H_T is the temperature scale height, $\chi_T = \frac{\partial}{\partial T} \left(\frac{4acT^3}{3\kappa\rho} \right)$, θ is the colatitude, $P_2(\cos \theta)$ is the Legendre polynomial of degree 2, and $\Theta = \frac{\tilde{\rho}}{\rho}$ represents the density fluctuation on an isobar and is proportional to the angular velocity gradient $\frac{\partial\Omega}{\partial r}$ (see § 5).

Combining Eqs. (3.56) and (3.51), we obtain the following expression for the total gravity :

$$\vec{g}_{\text{tot}} = \vec{g}_{\text{eff}} \left[1 - \frac{\kappa(\theta)L(P)(1 + \zeta(\theta))}{4\pi cGM \left(1 - \frac{\Omega^2}{2\pi G\rho_m}\right)} \right] = \vec{g}_{\text{eff}} (1 - \Gamma_\Omega(\theta)). \quad (3.57)$$

$\Gamma_\Omega(\theta)$ is called the local Eddington factor, defined as the ratio of the actual flux to the limiting local flux, and is used to define the $\Omega\Gamma$ limit.

From Eq. (3.57), we see that $\Gamma_\Omega(\theta)$ reaches a maximum when the opacity is maximum, which occurs at the equator where the temperature is lower. The $\Omega\Gamma$ limit is reached where $\Gamma_\Omega(\theta) = 1$ and when $\vec{g}_{\text{tot}} = \vec{0}$. This limit defines the break-up limit for luminous fast-rotating massive stars and should be the one considered when studying early-type stars (OB), Luminous Blue Variable stars (hereafter LBV), Red SuperGiants (hereafter RSG) and Wolf-Rayet stars (hereafter WR stars).

The radiative wind theory applied in the context described in this section leads the following expression for the total mass loss:

$$\frac{\dot{M}(\Omega)}{\dot{M}(0)} = \frac{(1 - \Gamma)^\frac{1}{\alpha} - 1}{\left[1 - \frac{\Omega^2}{2\pi G\rho_m}\right]^\frac{1}{\alpha} - \frac{1}{8} [1 - \Gamma]^\frac{1}{\alpha} - 1} \quad (3.58)$$

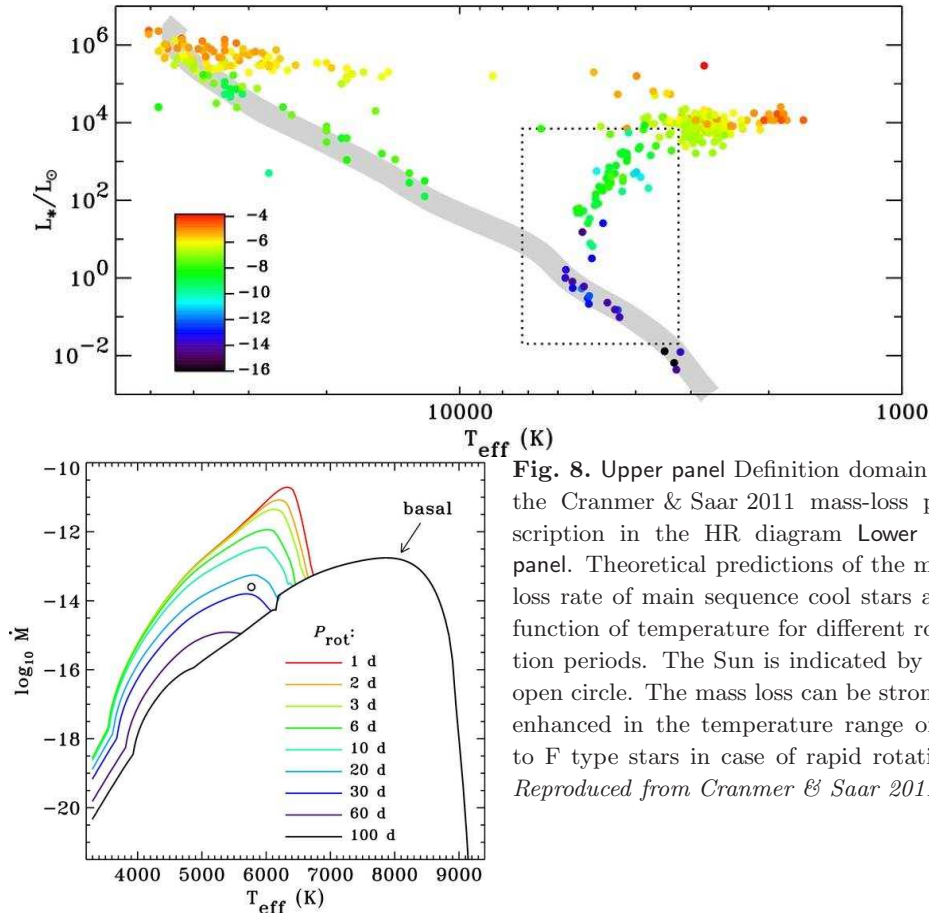


Fig. 8. Upper panel Definition domain for the Cranmer & Saar 2011 mass-loss prescription in the HR diagram Lower left panel. Theoretical predictions of the mass loss rate of main sequence cool stars as a function of temperature for different rotation periods. The Sun is indicated by the open circle. The mass loss can be strongly enhanced in the temperature range of G to F type stars in case of rapid rotation. *Reproduced from Cranmer & Saar 2011*

where $\Gamma_{\Omega} = \frac{\Gamma}{1 - \frac{\Omega^2}{2\pi G \rho_m}}$ with Γ the Eddington ratio corresponding to electron scattering opacity in a non-rotating star, and α is a force multiplier parameter that can be determined empirically (see Maeder 2009 for full details).

Using empirical force multipliers from the literature ($\alpha < 1$), Eq. (3.58) leads to very large mass loss for massive stars near classical break-up ($\Gamma \gtrsim 0.7$), in the domain of LBV stars, that should lead to the disruption of the star. For moderate rotation, the mass loss remains moderate.

3.4 Mass loss of cool low-mass rotating stars

Mass loss is an important process that can even drive the evolution of stars at certain phases of their lives. For massive stars, mass loss can be very strong

(this is the case during the WR and LBV phases for instance) and is driven by radiation processes. We have seen that it can be modified, actually amplified by rotation and will thus probably strongly affect the evolution of these stars (see § 6).

Moving now towards cooler lower mass stars, mass loss can be driven by (1) radiation pressure (with mass loss rates much lower than those reached by OB stars due to the lower temperature and luminosity), (2) acoustic waves (so-called *κ -mechanism*) for red giant stars and (3) vibrational instability in pulsating stars. For low-mass main sequence stars, the semi-empirical mass-loss prescription by Reimers (1975) is usually used, and it does not include any rotational effect :

$$\dot{M} = -3.98 \times 10^{-3} \eta \frac{L}{L_{\odot}} \frac{R}{R_{\odot}} \frac{M_{\odot}}{M} M_{\odot} \cdot yr^{-1} \quad (3.59)$$

with a parameter η calibrated in the range 1/3 to 3.

For long, this was one of the only prescription available to use in stellar evolution models of main sequence dwarfs, and for these objects it yields mass-loss rates in the range 10^{-15} to $10^{-13} M_{\odot} \text{ yr}^{-1}$ depending on the mass.

Cranmer & Saar (2011) have recently proposed a physically motivated model of time-steady mass loss suited to the case of cool main sequence and evolved giants (all late-type stars; see Fig. 8 upper panel), which can be used as an alternative to Eq. (3.59).

This model considers MHD fluctuations to be the only sources of energy and momentum to accelerate winds from cool stars. From this postulate, mass loss is then associated to supersonic winds emanating from (1) gas pressure in a hot corona, (2) wave pressure in a cool extended chromosphere, so that

$$\dot{M} \approx \dot{M}_{\text{cold}} + \dot{M}_{\text{hot}} \exp(-4M_{A,TR}) \quad (3.60)$$

where $M_{A,TR} = u/V_A$ is the Alfvén Mach number in the transition region between the cool chromosphere and the hot corona, u is the radial outflow speed of the wind, V_A is the Alfvén photospheric speed, directly proportional to the magnetic field strength and configuration, \dot{M}_{cold} is the chromospheric mass-loss rate and \dot{M}_{hot} is the hot coronal mass-loss rate.

The mass-loss rate thus depends directly on the magnetic field strength and configuration, which in turn depends on the rotation period P_{rot} . An approximate expression for this mass-loss rate would be :

$$\frac{\dot{M}}{10^{-10} M_{\odot} \text{ yr}^{-1}} \approx \left(\frac{R_*}{R_{\odot}} \right)^{16/7} \left(\frac{L_*}{L_{\odot}} \right)^{-2/7} \times \left(\frac{F_{A*}}{10^9 \text{ erg cm}^{-2} \text{ s}^{-1}} \right)^{12/7} f_*^{(4+3\theta)/7} \quad (3.61)$$

where f_* is the photospheric magnetic filling factor (associated to flux tubes that emerge in the chromosphere) that directly depends on the rotation period,

with $f_* \propto P_{rot}^{-1.8}$ (according to Saar 1996), θ is a dimensionless constant with values between 0 and 1, and F_{A*} is the flux of energy in kink/Alfvén waves in stellar photospheres.

This mass-loss rate prescription directly depends on rotation, and yields very good agreement with observations (for a sample of 29 stars with reliable measurements). In Fig. 8 we reproduce the predicted mass-loss rates as a function of effective temperature and rotational period P_{rot} . In the range $T_{eff} \in [3800K; 6700K]$, the mass-loss rates are very sensitive to the rotation period and can be greatly enhanced (up to 3 orders of magnitude) for rapid rotators.

Let us mention here that this prescription is not valid for (classical) T-Tauri stars, where the strong interaction of the star with its near environment implies a very intricate interplay between accretion and mass loss that remains to be fully understood (see J. Ferreira, this volume). It may nonetheless be used to model mass loss in weak T-Tauri stars (WTTS) for which the disk coupling and associated mechanisms are not dominant anymore (see J. Bouvier, this volume and § 6.4).

4 Transport processes in rotating stars

In the previous section we have seen how rotation modifies the basic stellar structure equations via the modification of the total potential by the centrifugal force, and the resulting modification of the radiative equilibrium of the rotating stars.

In addition to these *direct* effects, the fact that the star rotates also triggers hydrodynamical instabilities and large-scale motions of the plasma in the radiative regions, resulting in the transport of angular momentum and of chemical species. If the chemical stratification is modified in the regions where nucleosynthesis occurs, these transport processes are likely to affect the evolutionary path of the stars.

In this section, I briefly present the different physical transport processes that can exist in a rotating star (extended descriptions have been published in the proceedings of EES 2006 : see Talon 2008), and describe the formalisms developed to include them in 1D stellar evolution codes.

4.1 Hydrodynamical instabilities

According to the time-scales involved, we may separate the hydrodynamical instabilities that are likely to redistribute angular momentum and modify the abundance profiles in evolving stars in two classes :

- **Dynamical instabilities** – They operate on typical time-scales of the order of the free-fall time-scale $\tau_{ff} = \sqrt{\frac{R_*^3}{GM_*}}$, defined as the necessary time for a star to have its radius divided by 2. These instabilities thus act on very short time-scales and the associated perturbations can be considered to be adiabatic.

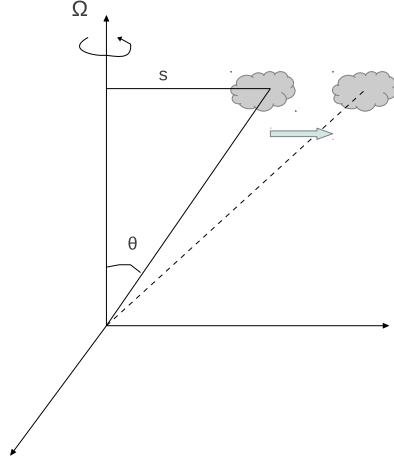


Fig. 9. Sketch of the configuration required for the Solberg-Høiland instability associated to the displacement of a fluid element in a rotating fluid, the direction of which is indicated by the arrow. $s = r \sin \theta$ is the distance to the rotation axis.

- **Secular instabilities** – They operate on typical time-scales of the order to the Kelvin-Helmholtz time-scale $\tau_{KH} = \frac{GM_*^2}{2R_*L_*}$, defined as the time for which a star can sustain its luminosity by the sole gravitational contraction. These instabilities act on time-scales of the order that of stellar evolution, and the associated perturbations are expected to allow energy exchange over nuclear time-scales. They should be explicitly accounted for.

4.1.1 Solberg-Høiland instability

This dynamical instability is related to Coriolis force and applies to a fluid in cylindrical rotation. It is also known as the axisymmetric baroclinic instability. It arises when the net force (gravity + buoyancy + centrifugal force) applied to a fluid parcel in an adiabatical displacement has components only in the direction of the displacement.

The stability criterion against axisymmetric displacements is twofold :

1. The Rayleigh stability criterion for a rotating fluid must be verified :

$$N^2 + N_{\Omega}^2 \sin^2 \theta \geq 0.$$

$$N^2 = N_T^2 + N_{\mu}^2 = \frac{g}{H_P} (\delta(\nabla_{\text{ad}} - \nabla) + \phi \nabla_{\mu}) \quad (4.1)$$

with $\delta = -(\partial \ln \rho / \partial \ln T)_{P,\mu}$ and $\phi = (\partial \ln \rho / \partial \ln \mu)_{P,T}$ the coefficients derived from the general equation of state (are unity for a perfect gas).

N is the Brunt-Väisälä frequency at which a fluid element oscillates when it is vertically adiabatically displaced (see Fig. 9). $N^2 > 0$ ensures the local stability against convection in non-rotating fluid.

$$N_{\Omega}^2 = \frac{1}{s^3} \frac{d(s^4 \Omega^2)}{ds} \quad (4.2)$$

defines the Rayleigh frequency associated to the Rayleigh criterion defining the stability of an angular velocity distribution in a fluid.

2. The specific angular momentum $j = s^2 \Omega$ increases outward (e.g. increases from pole to equator along isentropic surfaces (S constant)).

In the non-rotating case, the Ledoux stability criterion for convection is recovered.

Rotation has a stabilizing effect against convection provided $dj/ds > 0$.

The Solberg-Høiland instability is a baroclinic instability that develops for axisymmetric and adiabatic perturbations only if the Rayleigh criterion ($N_{\Omega}^2 > 0$) is violated. It occurs only in regions with decreasing specific angular momentum gradient and is efficiently quenched in stably stratified regions (where $\nabla < \nabla_{ad} + \frac{\phi}{\delta} \nabla \mu$). *It evolves on a dynamical characteristic time-scale.*

4.1.2 Baroclinic instabilities

These instabilities can develop in the radiative regions of stars experiencing non-cylindrical rotation laws, that is in *baroclinic radiative stellar interiors*.

They are related to axisymmetric perturbations of the fluid and act on secular time-scales. Only *linear* stability criteria exist to describe them. These criteria can be viewed as modifications of the Solberg-Høiland criterion when the weakening effect of thermal diffusivity on the stabilizing effect of the temperature gradient (GSF instability) and the weakening effect of molecular diffusivity on the stabilizing effects of the chemical stratification (ABCD instability) are taken into account :

- GSF instability criterion (Goldreich & Schubert 1967, Fricke 1968, Acheson 1978) for axisymmetric perturbation of a rotating fluid with finite viscosity ν and thermal diffusivity K_T :

$$\frac{\nu}{K_T} N_T^2 + N_{\mu}^2 < 0 \quad \text{or} \quad \left| s \frac{\partial \Omega}{\partial z} \right|^2 > \frac{\nu}{K_T} N_{T,ad}^2$$

- ABCD instability criterion (Knobloch & Spruit 1983) :

$$\frac{\nu}{K_T} (N_T^2 + N_{\mu}^2) + N_{\Omega}^2 < 0.$$

These instabilities are hindered by large Prandtl numbers $\mathcal{P} = \frac{\nu}{\kappa_{\tau}}$, which is the case when horizontal turbulence is strong.

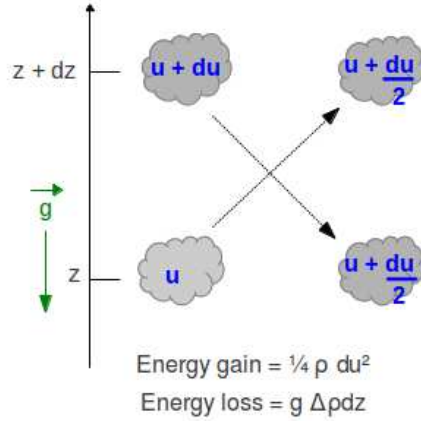


Fig. 10. Sketch illustrating the shear instability according to Richardson criterion.

4.1.3 Shear instability

The stability of a differentially rotating fluid against shear is determined by the Richardson criterion :

$$Ri \equiv \frac{N^2}{(du/dz)^2} > Ri_{\text{crit}} = \frac{1}{4} \quad (4.3)$$

where u is the velocity of the fluid elements (“*eddies*”) and z designates the vertical direction as illustrated on Fig. 10.

It defines the ability of the entropy gradient to stabilize a radiative region and is hindered by density stratification. This criterion was derived by Chandrasekhar (1961) from energy considerations, and is thus representative of *non-linear* regimes.

Dynamical shear instability : horizontal turbulence

Along isobars, no restoring force exist and the shear is free to develop and becomes turbulent whenever horizontal differential rotation is present. The horizontal shear is a dynamical shear instability, acting on *dynamical time-scales* and leading to a large horizontal turbulent viscosity that ensures shellular rotation.

Very little is known about the non-linear regime of the shear instability, but from laboratory experiments, turbulence seems to have a tendency to suppress its cause, that is differential rotation when the turbulence results from shear (Richard & Zahn 1999). Assuming that the same occurs in stellar radiation zones Zahn (1992) proposed that the main role of the horizontal turbulent viscosity ν_h is to smooth out horizontal shear produced by the advection of angular momentum through the meridional circulation.

Three prescriptions, derived from laboratory experiments (Mathis et al. 2004), energetic considerations (Maeder 2003), or relying on arbitrary postulates (Zahn 1992), are available to express the horizontal shear turbulent viscosity as a function of the

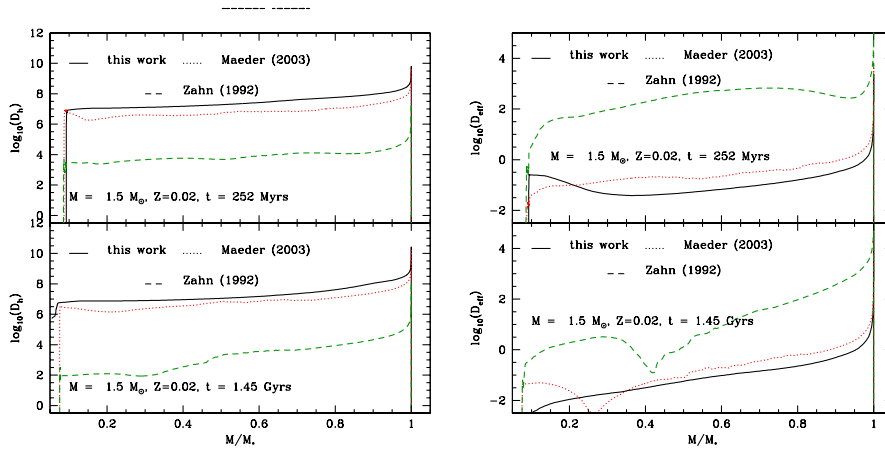


Fig. 11. Horizontal turbulent shear diffusivity (*left*) and effective diffusivity (*right*) profiles at two different ages in a $1.5 M_{\odot}$ rotating model at solar metallicity. *Figure from Mathis et al. (2007)*

meridional circulation (defined hereafter in § 4.2), and we give their expressions here :

- Zahn (1992)

$$\nu_h = \frac{r}{C_h} \left| \frac{1}{3\rho r} \frac{d(\rho r^2 U)}{dr} - \frac{U}{2} \frac{d \ln r^2 \Omega}{d \ln r} \right| \equiv \frac{r}{C_h} |2V - \alpha U|, \quad (4.4)$$

where C_h is a free parameter of order 1, $V = \frac{1}{6\rho r} \frac{d}{dr} (\rho r^2 U)$ is the horizontal component of the meridional velocity, U is the vertical component of the meridional velocity (see hereafter); and $\alpha = \frac{1}{2} \frac{d \ln r^2 \Omega}{d \ln r}$.

- Maeder(2003) and Mathis et al. (2004)

$$\nu_h = \chi^{\frac{1}{n}} r (r \bar{\Omega}(r) V^k [2V - \alpha U])^{\frac{1}{n}}, \quad (4.5)$$

where $(\chi ; n ; k) = (\frac{3}{400m\pi} ; 3 ; 1)$ in Maeder's expression (with $m = 1, 3$ or 5), and $(1.610^{-6} ; 2 ; 0)$ in Mathis et al. (2004).

In Fig. 11, we reproduce the profiles of the horizontal shear diffusivity assimilated to the horizontal shear viscosity ($\nu_h \equiv D_h$) for the three prescriptions above, for the case of a low-mass main sequence star with a surface velocity of 110 km.s^{-1} on the Zero Age Main Sequence (hereafter ZAMS). The more recent prescriptions by Maeder (2003) and Mathis et al. (2004) predict a similar and much stronger horizontal shear (by 4 orders of magnitude!) in the differentially rotating radiative interior of this star. This strongly impacts the transport of nuclides as can be seen on the right panel of the same figure. There the effective diffusion coefficient

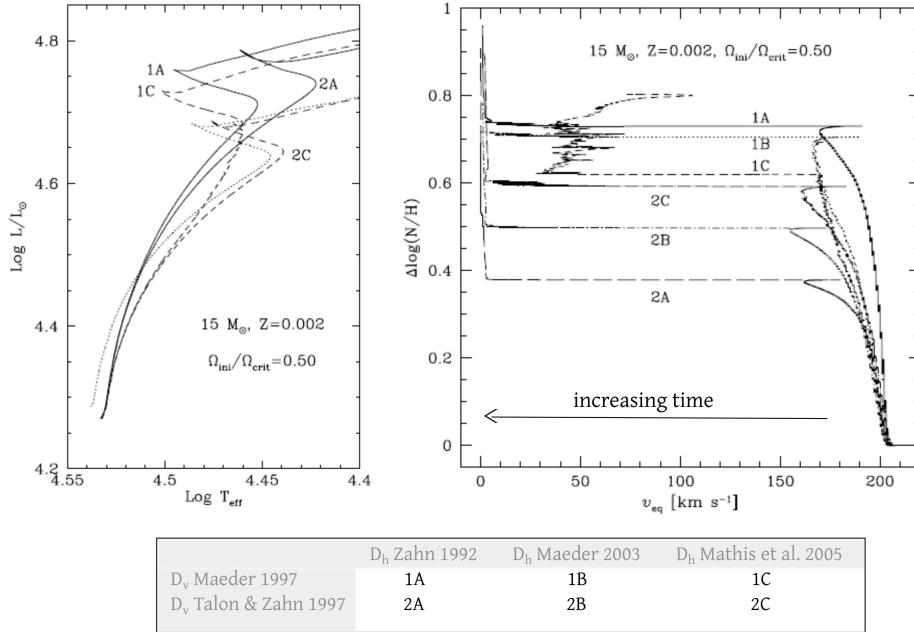


Fig. 12. Influence of the adopted prescriptions for the horizontal and vertical shear turbulent diffusion coefficient on the evolution and surface abundances of a $15 M_{\odot}$ model at low metallicity and moderate rotation. *Adapted from Meynet et al. 2013.*

profiles associated to the transport of nuclides by the meridional circulation (see below and Chaboyer & Zahn 1992) are presented and are up to 2 orders of magnitude lower for these prescriptions of D_h .

Let us finally underline that the dynamical shear instability as defined by the sole Richardson criterion does not account for the thermal effects and will thus only develop in fluids that have a large Peclet number $Pe = \frac{v\ell}{K_T}$ that is the ratio of the thermal to the dynamical time-scales for v a typical velocity and ℓ the typical length scale of fluid elements. As such it is thus expected to develop only in the late evolutionary phases of rotating massive stars, being hindered by the buoyancy in most of the cases.

Secular shear instability : vertical turbulence

Shear instability can also develop in stellar interiors over *secular time-scales*.

While on isobars the shear instability is free to grow, in the direction of entropy stratification, the thermal and chemical stratifications prevent the instability to develop. However, when the horizontal shear is fully developed so that $\nu_h \gg \nu_v$, it contributes to weaken the stabilizing effect of stratification, as does thermal dif-

fusivity. A modified instability Richardson criterion was first proposed by Maeder (1997) to incorporate the destabilizing effects of thermal diffusivity and it was further extended by Talon & Zahn (1997) to yield :

$$\left(\frac{\Gamma}{\Gamma+1}\right)N_T^2 + \left(\frac{\Gamma_\mu}{\Gamma_\mu+1}\right)N_\mu^2 < Ri_{\text{crit}}\left(\frac{du}{dz}\right)^2 \quad (4.6)$$

where $\Gamma = v\ell/K_T$ and $\Gamma_\mu = v\ell/K_\mu$. Γ may be understood as a turbulent Peclet number, where the turbulent viscosity replaces the usual molecular viscosity. Ri_{crit} is usually considered to be 1/4 as in the classical Richardson criterion, but values of 1/6 or values closer to the unity can be found in the literature (Canuto 1998). Let us emphasize that the criterion enunciated in Eq. (4.6) derives from energy considerations and as such also *describes the non-linear (turbulent) growth of the instability*.

In order for the secular shear instability to grow, another criterion must be complied, ensuring that the associated turbulent viscosity ν_v is larger than the microscopic viscosity of the medium. This condition is known as the Reynolds instability criterion

$$\nu_v \geq \nu \mathcal{R}e_c \quad (4.7)$$

where $\mathcal{R}e_c$ is the critical Reynolds number beyond which turbulence can develop freely and is not damped any more by the fluid's viscosity. In stellar evolution codes, $\mathcal{R}e_c = 10$ is generally adopted.

Finally an expression for the vertical shear turbulent viscosity ν_v can be obtained from Eq. (4.6) (Talon & Zahn 1997):

$$\nu_v = \frac{1}{4} \frac{Ri_c \left(s \frac{d\Omega}{dr}\right)^2}{\frac{N_T^2}{K_T + \nu_h} + \frac{N_\mu^2}{\nu_h}} \quad (4.8)$$

with $s = r \sin \theta$.

Figure 12 shows the effect of the different possible combinations of prescriptions for the vertical and horizontal shear turbulent diffusion coefficients (Meynet et al. 2013). The evolutionary tracks and the surface enrichments predicted for a given initial rotation rate are significantly affected by the choice of these prescriptions. Comparison between models using different descriptions for the rotation-driven instabilities should be done with caution. Actually, this kind of parameter-space exploration gives a hint on theoretical errorbars one should keep in mind when using stellar evolution models that have been computed with specific prescriptions and physical inputs.

As seen from the list above, rotation-driven instabilities are numerous. Unfortunately most of them lack a reliable description in their non-linear regime. This is a crucial point since mixing and transport by hydrodynamical instabilities occur

via the turbulence they generate, and turbulence occurs in the non-linear regime. For those hydrodynamical instabilities that lack a non-linear criterion (the baroclinic instabilities including the Solberg-Høiland instability for instance), caution is advised when evaluating the amount of mixing they may generate from linear instability criteria.

The instability criterion derived for the shear instability on the other hand comes from energy considerations and can be applied to the *non-linear* regime. This ensures a better grounded evaluation of the mixing generated by shear in stellar radiative interiors.

4.2 Meridional circulation

Meridional circulation occurs in convective and radiative regions in stars, and we focus here on the radiative regions. It was first introduced to solve the so-called *Von Zeipel paradox* by Eddington (1925) and Vogt (1925).

When considering the equilibrium of a rotating radiative region, von Zeipel (1924) noticed that “*a rotating star cannot achieve simultaneously hydrostatic equilibrium and solid-body rotation*”. This can be easily seen combining the energy conservation equation and the hydrostatic equilibrium in spherical coordinates for the axisymmetric case, with solid-body rotation :

$$\vec{\nabla} \cdot \vec{F} = \frac{d}{d\Psi} \left(\chi(\Psi) \frac{dT}{d\Psi} \right) (\vec{\nabla}\Psi)^2 + \chi(\Psi) \frac{dT}{d\Psi} \Delta\Psi + \rho\epsilon = 0 \quad (4.9)$$

In this equation Ψ is the total potential (gravitational + centrifugal) and in the barotropic case considered, $\vec{\nabla}\Psi$ is the effective gravity which is not constant on equipotentials, contrary to the other terms in $\frac{dT}{d\Psi}$. This leads to the necessity for the energy generation to depend on the angular velocity, which did not suit Eddington and Vogt. They simultaneously proposed in 1925 a solution to the Von Zeipel paradox that would not require any specific form for the energy generation, by introducing the advection of entropy in the heat equation

$$\rho T \vec{U} \cdot \vec{\nabla} S = \vec{\nabla} \cdot (\chi \vec{\nabla} T) + \rho\epsilon \quad (4.10)$$

where \vec{U} is the meridional circulation velocity. Meridional circulation carries away the excess energy from warm regions and brings energy to the otherwise cooling regions. Although very largely adopted as the correct solution to von Zeipel paradox, this formulation is not correct as first shown by Zahn (1992) and as clearly explained by Rieutord (2008) (see also S. Mathis in this volume). It is nonetheless still in use to model meridional circulation in some stellar evolution codes (see Endal & Sofia 1978, Pinsonneault et al. 1989, Heger et al. 2000).

Assuming strong anisotropic shear turbulence that ensures that the horizontal shear viscosity (along the isobars) is much larger than the vertical shear viscosity, $\nu_h \gg \nu_v$, the heat equation must be complemented by an horizontal heat

flux \vec{F}_h that creates a thermal imbalance. This imbalance is compensated by the advection of entropy, introducing here the meridional circulation (see Zahn 1992, Maeder & Zahn 1998 for complete description) :

$$\rho T \vec{U} \cdot \vec{\nabla} S = \vec{\nabla} \cdot (\chi \vec{\nabla} T) + \rho \varepsilon - \vec{\nabla} \cdot \vec{F}_h. \quad (4.11)$$

\vec{F}_h can be approximated by

$$\vec{F}_h = -\nu_h \rho T \vec{\nabla} S \approx -\nu_h \rho C_p \vec{\nabla}_h T.$$

The meridional circulation velocity is a vector field that can be expanded over spherical functions for axisymmetric fields:

$$\vec{U} = \underbrace{\sum_{l>0} U_l(r) P_l(\cos \theta)}_{U_r} \vec{e}_r + \underbrace{\sum_{l>0} V_l(r) \frac{dP_l(\cos \theta)}{d\theta}}_{U_\theta} \vec{e}_\theta, \quad (4.12)$$

where P_l is the Legendre polynomial of order l . Stopping the expansion at the second order, we get

$$\vec{U} = U_2(r) P_2(\cos \theta) \vec{e}_r + V_2(r) \frac{dP_2(\cos \theta)}{d\theta} \vec{e}_\theta. \quad (4.13)$$

U_2 and V_2 depend on the radius of the isobar only, which is very convenient for the introduction of this formalism into 1D stellar evolution code, and their expressions are as follows (see Zahn 1992, Maeder & Zahn 1998 for full derivation) :

$$V_2 = \frac{1}{6\rho r} \frac{d(r^2 \rho U_2(r))}{dr} \quad \text{from continuity equation} \quad (4.14)$$

$$U_2 = \frac{P}{\rho g C_P T} \frac{1}{(\nabla_{\text{ad}} - \nabla + \nabla_\mu)} \left[\frac{L}{M} (E_\Omega + E_\Theta + E_\mu) + \frac{TC_P}{\delta} \frac{\partial \Theta}{\partial t} \right] P_2(\cos \theta) \quad (4.15)$$

From Eq. (4.11).

Here $\Theta = \frac{\tilde{p}}{\bar{p}} = \frac{r^2}{3g} \frac{\partial \Omega^2}{\partial r}$ describes the density fluctuation on the isobar of radius $r \equiv r_P$, and $g \equiv g_{\text{eff}}$ is the effective gravity as defined by Eq. (3.45). E_Ω , E_Θ and E_μ are terms depending explicitly on the angular velocity profile, density, and mean molecular weight fluctuations on an isobar respectively.

Meridional circulation transports both angular momentum and nuclides, as the hydrodynamical instabilities described earlier. Within the framework of shellular rotation, its action on nuclides can be assimilated to a diffusion process. The associated diffusion coefficient was derived by Chaboyer & Zahn (1992):

$$D_{\text{eff}} = \frac{|rU_2|^2}{30D_h} \quad (4.16)$$

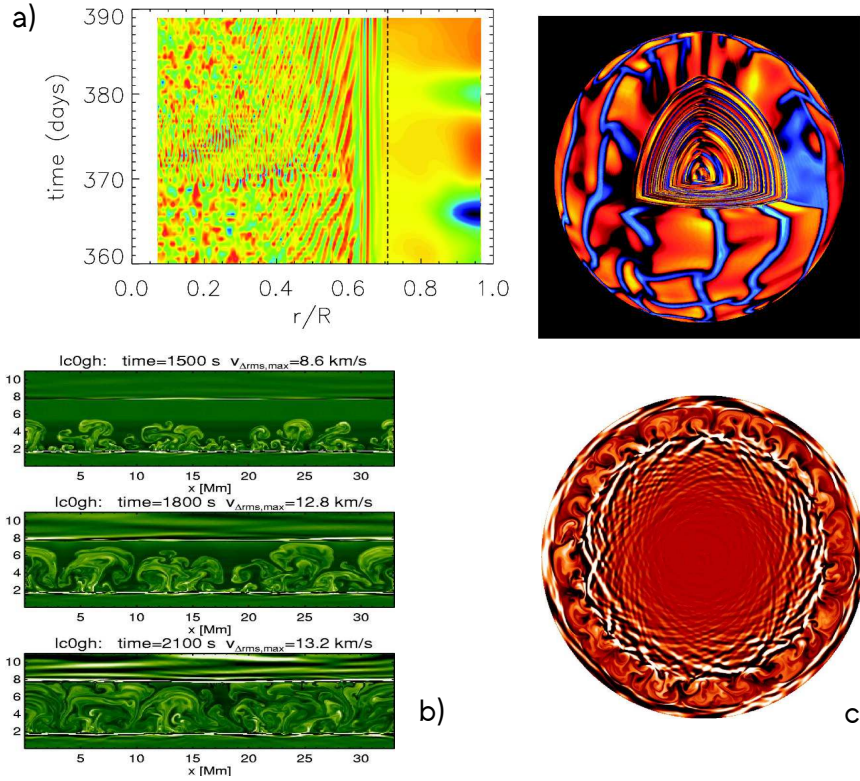


Fig. 13. Internal gravity waves in 2-D and 3-D MHD simulations. a) In the Sun (*From Alvan et al. 2012*). b) Propagation of IGW in the radiative layer above the convectively unstable helium burning region developing during the He flash in a low-mass red giant star (*From Herwig et al. 2006*). c) IGW propagating below the solar convection zone as obtained in a 2-D hydrodynamical simulation (*From Rogers et al. 2006*).

4.3 Internal Gravity Waves

Contrary to hydrodynamical instabilities or to meridional circulation which are *rotation-driven* transport processes, internal gravity waves (hereafter IGW) exist and propagate in stellar interiors even in the absence of rotation. Rotation however affects their damping and propagation, making IGW important vectors for the transport of angular momentum.

The reader is referred to Talon (1998) and to Maeder (2009) for an in depth introduction to IGW. A brief phenomenological description of IGW is given in this section together with a more detailed and updated description of the available formalism to introduce these waves as an additional angular momentum transport process in 1-D stellar evolution codes.

Fluid displacements generated by convective motions in the underlying stable and stratified radiative regions lead to the oscillation of the fluid elements displaced, thus yielding the propagation of IGW. Gravity and buoyancy are the restoring forces for these waves, which means that a favoured direction of propagation exists. When trapped in cavities, waves are referred to as *g-modes*. The IGW denomination is usually reserved to evanescent gravity waves.

Fig. 13 shows the results of hydrodynamical simulations for the Sun (sub-panels a and b) and in a red giant star during the helium flash (sub-panel c), where the generation of IGW is clearly seen in the radiative stable layers surrounding the convective regions where convection is fully developed.

Propagating vertically and horizontally in the fluid *IGW transport energy and angular momentum in stratified media*. As the natural oscillation frequency of a displaced fluid element in a stratified medium is the Brunt-Väisälä frequency N (see Eq. 4.1), their frequency σ is necessarily lower than N with

$$0 < \sigma < N.$$

The excitation processes of IGW are twofold (1) convective overshooting in a stable region and (2) excitation by the Reynolds stresses in the convection zone itself. The mechanism preferentially chosen within the framework of IGW propagation and damping modelling in stellar evolution codes is the later one because it has the advantage of being fully described by a formalism developed by Goldreich et al. (1994).

Using this formalism and considering that IGW are purely gravity waves, the kinetic energy flux per unit frequency for IGW writes (see Talon & Charbonnel 2005):

$$\begin{aligned} \mathcal{F}_E(\ell, \omega) &= \frac{\omega^2}{4\pi} \int dr \frac{\rho^2}{r^2} \left[\left(\frac{\partial \xi_r}{\partial r} \right)^2 + \ell(\ell+1) \left(\frac{\partial \xi_h}{\partial r} \right)^2 \right] \\ &\times \exp \left[-h_\omega^2 \ell(\ell+1)/2r^2 \right] \frac{v_c^3 L^4}{1 + (\omega\tau_L)^{15/2}} \end{aligned} \quad (4.17)$$

with ξ_r and $[\ell(\ell+1)]^{1/2}\xi_h$ the radial and horizontal displacement wave functions normalized to unit energy flux at the edge of the considered convection zone, v_c the convective velocity, $L = \alpha_{\text{MLT}} H_P$ the radial size of an energy bearing turbulent eddy, $\tau_L \approx L/v_c$ the characteristic convective time, H_P the pressure scale height $P/\rho g$, and h_ω the radial size of the largest eddy at depth r with characteristic frequency of ω or higher ($h_\omega = L \min\{1, (2\omega\tau_L)^{-3/2}\}$). The radial and horizontal wave numbers (respectively k_r and k_h) are related by

$$k_r^2 = \left(\frac{N^2}{\omega^2} - 1 \right) k_h^2 = \left(\frac{N^2}{\omega^2} - 1 \right) \frac{\ell(\ell+1)}{r^2} \quad (4.18)$$

where N^2 is the Brunt-Väisälä frequency.

According to Unno et al. (1989), for the waves in the low-frequency range ($\sigma \ll N$),

the dispersion relation is given by

$$k^2\sigma^2 + N^2k_h^2 = 0. \quad (4.19)$$

where $\sigma = \omega - m[\Omega(r) - \Omega_{CZ}]$ is the local Doppler-shifted frequency of the wave, and ω is the wave frequency in the reference frame of the convective zone where the angular velocity Ω_{CZ} is assumed to be constant.

Using the energy flux defined in Eq. (4.17), it is possible to establish the so-called "angular momentum luminosity" at the edge of the convective region generating the IGW

$$\mathcal{L}_J(\ell, m) = 4\pi r^2 \mathcal{F}_J(\ell, m, \omega) = 4\pi r^2 \frac{2m}{\omega} \mathcal{F}_E(\ell, \omega) \quad (4.20)$$

where $\mathcal{F}_J(\ell, m, \omega)$ is the mean flux of angular momentum carried by a monochromatic wave of spherical order ℓ and local (i.e., emission) frequency ω (m being the azimuthal order).

IGW are prone to radiative damping by thermal diffusivity and viscosity in corotation resonance (see Zahn et al. 1997), and deposit the angular momentum they carry at the location where they are damped. Angular momentum deposition can be positive or negative depending on the nature in terms of prograde or retrograde (azimuthal number $m > 0$ or < 0 respectively). In the absence of differential damping for prograde and retrograde waves, there will be no net local excess or deficit of angular momentum.

The local momentum luminosity at a given radius r within a *differentially rotating* radiative region where the waves propagate, accounts for prograde and retrograde waves generated by the convective zone and is given by

$$\mathcal{L}_J(r) = \sum_{\sigma, \ell, m} \mathcal{L}_{J\ell, m}(r_{cz}) \exp[-\tau(r, \sigma, \ell)]. \quad (4.21)$$

Here the 'cz' index corresponds to the radiation/convection interface, and $\tau(r, \sigma, \ell)$ is the local damping rate given by

$$\tau(r, \sigma, \ell) = [\ell(\ell + 1)]^{3/2} \int_r^{r_c} (K_T + \nu_v) \frac{NN_T^2}{\sigma^4} \left(\frac{N^2}{N^2 - \sigma^2} \right)^{1/2} \frac{r}{r^3} \quad (4.22)$$

where σ is the Doppler-shifted frequency defined earlier, K_T is the thermal diffusivity, ν_v is the vertical shear turbulent viscosity (see § 4.1) and N_T^2 is the thermal part of the Brunt-Väisälä frequency (see Eq. 4.1).

When Coriolis forces are neglected (no gravito-inertial waves), Eq. (4.21) and (4.22) indicate that low-frequency ($\sigma \ll N$), low-degree (small ℓ) IGW are the ones efficient to redistribute angular momentum in the radiative interiors. They

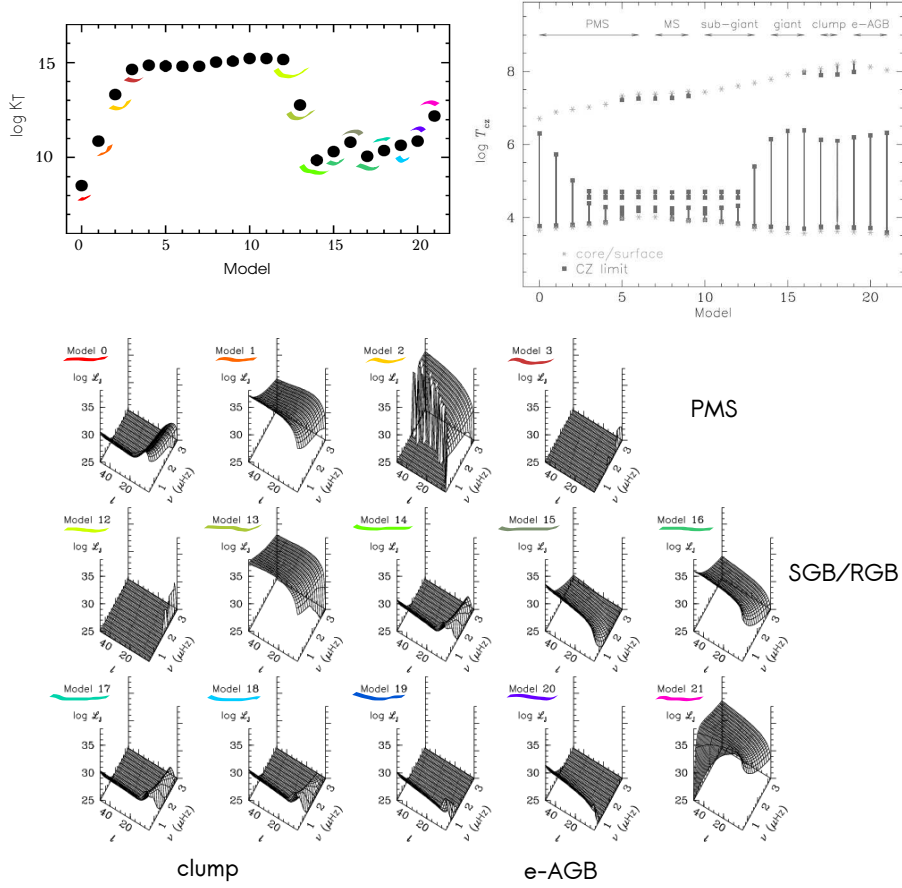


Fig. 14. Thermal diffusivity, temperature at the surface and the convective edges, and spectrum of angular momentum luminosity integrated over $0.2 \mu\text{Hz}$ in a $3M_{\odot}$ model at solar metallicity at different evolutionary points from the PMS to the early-AGB. (Adapted from Talon & Charbonnel 2008.)

penetrate in the deepest radiative layers and their prograde and retrograde components are subject to strong differential damping, which is required for a net angular momentum deposition (or extraction). *This differential damping is due to the differential rotation present in the radiative interiors* (see Zahn et al. 1997, Talon & Charbonnel 2003, Talon & Charbonnel 2005, Talon & Charbonnel 2008, Charbonnel et al. 2013). Equations also show that the actual efficiency of IGW to angular momentum redistribution strongly depends on the physical conditions at the edge of the convective regions, which in turn depend on the surface temperature of the star. For instance, the IGW angular momentum luminosity is

reduced for shallow convective envelopes at the base of which the thermal diffusivity is large, leading to an efficient damping very close to the convective edge (see Talon & Charbonnel 2008 and Fig. 14 adapted from the same paper).

Pantillon et al. (2007) provide modified expressions of $\mathcal{L}_{\mathcal{J}}$ when accounting for the Coriolis acceleration and the fact that not only pure gravity-waves but also gravito-inertial waves are generated and propagate in the radiative regions. They use the “*traditional approximation*” where the radial component of the Coriolis acceleration is neglected in the equation of motion of the fluid.

In that case, the dispersion relation (Eq. 4.19) and the total angular momentum luminosity (Eq. 4.21) associated to the waves are modified. Further modifications also appear when Lorentz forces are also accounted for in presence of a stellar magnetic field (see Mathis & de Brye 2012).

5 Modelling rotation-induced mixing in stellar evolution codes

In the previous sections we have seen how rotation itself, rotation-driven and rotation-influenced processes can modify the stellar structure, the stellar radiative equilibrium, and generate transport of angular momentum inside radiative regions essentially. We have also described different formalisms that have been developed across the years to model rotation in 1-D stellar evolution codes.

Here we put together the two main approaches that have been implemented in these very same 1-D stellar evolution codes to account for the transport of angular momentum and nuclides by rotation-driven and rotation-influenced physical processes.

5.1 Diffusive approach

This approach was first proposed by Endal & Sofia (1978) in their seminal paper. It is used in the stellar evolution codes KEPLER (Heger et al. 2000), STERN (Yoon & Langer 2005) and MESA (Paxton et al. 2013). The angular momentum and nuclides profiles evolution due to secular rotation-driven instabilities are described by a set of two diffusion equations, which have the advantage to be computationally easy to implement :

$$\frac{\partial \Omega}{\partial t} = \frac{1}{\rho r^4} \frac{\partial}{\partial r} \left(\rho r^4 \nu \frac{\partial \Omega}{\partial r} \right) \quad (5.1)$$

$$\frac{\partial X_i}{\partial t} = \frac{1}{\rho r^2} \frac{\partial}{\partial r} \left(\rho r^2 D \frac{\partial X_i}{\partial r} \right) \quad (5.2)$$

where X_i is the mass fraction of nuclide i , ν and D are respectively the total viscosity and the total diffusion coefficient defined as a sum of all diffusion coefficients associated to the transport processes taken into account. Each of these diffusion coefficients is built as the product of the velocity v and the path length l of the

redistribution currents with

$$l = \min \left(r, \left| \frac{\partial r}{\partial \ln v} \right| \right). \quad (5.3)$$

$\left| \frac{\partial r}{\partial \ln v} \right|$ is the velocity scale height. The time-scale associated to the *redistribution* over path scale is then simply $l^2/D = l/v$.

With this description, the viscosity ν is given by

$$\nu = D_{\text{conv}} + D_{\text{sem}} + D_{\text{SSI}} + D_{\text{DSI}} + D_{\text{SHI}} + D_{\text{ES}} + D_{\text{GSF}} \quad (5.4)$$

and the diffusion coefficient is usually written as the following sum (Heger et al. 2000)

$$D = D_{\text{conv}} + D_{\text{sem}} + f_c \times (D_{\text{SSI}} + D_{\text{DSI}} + D_{\text{SHI}} + D_{\text{ES}} + D_{\text{GSF}}) \quad (5.5)$$

f_c is one of the efficiency parameters entering the diffusive formalism. It is defined as the ratio of the diffusion coefficient to the turbulent viscosity $f_c \equiv D/\nu$ and it is calibrated on observations (solar lithium abundance in Pinsonneault et al. 1989, nitrogen abundances at the surface of B-type in the LMC in Brott et al. 2011a). Another parameter, f_μ ($\in [0; 1]$) is introduced to mimic the sensitivity of the rotationally induced mixing to μ -gradients, i.e., ∇_μ is replaced by $f_\mu \nabla_\mu$.

These parameters were introduced by Pinsonneault et al. (1989) to account for the “*considerable uncertainties*” (as explicitly written in Heger et al. 2000) associated to diffusion coefficient used as they derive from order-of-magnitude considerations.

The equation for the angular momentum evolution describes the angular velocity at all radii inside the star, with no distinction between radiative and convective regions. In the latter, solid-body rotation is assumed and actually results from the very large convective diffusion coefficient D_{conv} associated to the very short time-scales characterizing convection.

This equation can be modified to include the presence of a surface torque, for instance as that exerted by a disc coupling or a magnetized wind. We address this specific point in § 5.3 (see also J. Ferreira and J. Bouvier, this volume).

5.2 Combined advective/diffusive approach

The other family of stellar evolution models including rotation adopts the formalism developed by Chaboyer & Zahn (1992), Zahn (1992) and Maeder & Zahn (1998), in which only the transport of nuclides is modelled with a diffusion equation, but the evolution of the angular momentum obeys an advection/diffusion equation. This formalism is used in the STAREVOL (Palacios et al. 2006, Decressin et al. 2009), CESTAM (Marques et al. 2013) and Geneva stellar evolution codes (Meynet & Maeder 1997, Eggenberger et al. 2008). It is also included in a simplified hybrid form in the FRANEC stellar evolution code (Chieffi & Limongi 2013).

The transport equations governing the evolution of angular momentum and nuclides *in the radiative interior* read :

$$\rho \frac{d}{dt} [r^2 \Omega] = \underbrace{\frac{1}{5r^2} \frac{\partial}{\partial r} [\rho r^4 \Omega U]}_{ADVECTION} + \underbrace{\frac{1}{r^4} \frac{\partial}{\partial r} \left[\rho \nu_v r^4 \frac{\partial \Omega}{\partial r} \right]}_{DIFFUSION} + \underbrace{\frac{3}{8\pi r^2} \frac{\partial \mathcal{L}_J}{\partial r}}_{IGW} \quad (5.6)$$

$$\rho \frac{dc}{dt} = \underbrace{\rho \dot{c}}_{nuclear} + \underbrace{\frac{1}{r^2} \frac{\partial}{\partial r} [r^2 \rho V_{ip} c]}_{microscopicproc.} + \underbrace{\frac{1}{r^2} \frac{\partial}{\partial r} \left[r^2 \rho (D_{eff} + D_v) \frac{\partial c}{\partial r} \right]}_{shear+merid.circ.} \quad (5.7)$$

where c_i is the concentration of nuclide i , and V_{ip} is the microscopic diffusion velocity of nuclides of species i with respect to protons.

These equations need to be complemented by an equation describing the evolution of the mean molecular weight relative fluctuations $\Lambda = \frac{\tilde{\mu}}{\bar{\mu}}$ on an isobar. As for the nuclides abundances/concentrations/mass fractions, we can write a diffusion equation for the evolution of the mean molecular weight μ on an isobar provided that we write it using the perturbative approach $\mu = \bar{\mu} + \tilde{\mu} P_2(\cos \theta)$:

$$\frac{\partial \tilde{\mu}}{\partial t} + U_2 \frac{\partial \tilde{\mu}}{\partial r} = \frac{6}{r^2} D_h \tilde{\mu} \quad (5.8)$$

which can be re-written into an equation for Λ :

$$\frac{\partial \Lambda}{\partial t} = \frac{U_2}{H_P} \nabla_\mu - \frac{6}{r^2} D_h \Lambda \quad (5.9)$$

With this advective/diffusive description of the angular momentum transport in the *radiative stellar interiors*, at each evolutionary time-step, it is necessary to solve a coupled system of five non-linear differential equations resulting from the splitting of the 4th order in Ω of the angular momentum transport equation (Eq. 5.6) + the equation for mean molecular weight fluctuations evolution (Eq. 5.9). This set of equations is complemented by boundary equations that include in particular the expression of the torque exerted by a wind for young low- and intermediate-mass stars.

The convective regions are assumed to have a solid-body rotation, they are treated as a bulk by integrating their inertia momentum at each time-step, and serve as boundary conditions to the radiative interior equations. The diffusion equation for nuclides (Eq. 5.7) is also solved at each time-step.

5.3 Interaction with the environment during early evolution

As indicated in the previous subsections, the transport of angular momentum, whether it is modeled by a diffusion or an advection/diffusion formalism, needs to be complemented by other mechanisms than the hydrostatic effects and the

rotation-driven/influenced instabilities, that should also play a role in redistributing angular momentum.

This paper appears in the proceedings of the Evry Schatzman School 2012 on “*Angular momentum transport mechanisms and their role on the formation and early evolution of stars*”, where several contributions (J. Ferreira, J. Bouvier, S. Fromang) discuss the interaction between the low-and intermediate-mass stars with their environment during the T-Tauri phase.

The star is then surrounded by a disk with which it strongly interacts. In addition young stars appear to be highly magnetized, which reinforces the star-disk interaction and deeply influences the stellar winds. Facing the profound complexity of these processes, which undoubtedly play a major role in the angular momentum evolution during the early evolution phases, we lack from a consistent formalism to incorporate in stellar evolution codes.

Accretion of matter (and of angular momentum) from the disk onto the star is an important process that can alter the evolutionary paths, the ages and the angular momentum evolution of low-mass stars on the pre-main sequence. Yet this process is generally not accounted for when computing stellar evolution models for stars with $M_{\text{ini}} \geq 0.6 M_{\odot}$ with some exceptions (Palla & Stahler 1992, Palla & Stahler 1993, Siess & Forestini 1996, Siess et al. 1997, Siess et al. 1999, Tout et al. 1999, Baraffe et al. 2009). Note that for accretion rates of about $10^{-7} M_{\odot} \text{yr}^{-1}$, the influence of this process is negligible on the stellar tracks and ages. Its influence on the global angular momentum evolution is on the other end yet to be explored.

To summarize it in one word, the T-Tauri (Classical T-Tauri phase) is not properly taken into account in stellar evolution codes as far as the angular momentum evolution is concerned. During this phase, and based on empirical (observational) evidence (see J. Bouvier in this volume), stellar evolution models just enforce the surface angular velocity to remain constant for a variable duration corresponding to what is abusively called “disc-coupling”.

When reaching the more advanced weak T-Tauri phase, the star-disk interaction is much weaker and there, several prescriptions exist for the stellar wind torque that is exerted at the stellar surface. The first popular prescription is based on extrapolation of a fit to a mean rotation velocity of stars in the Pleiades, Ursa Major, the Hyades and of the Sun as a function of age (Skumanich 1972). This law is of the form:

$$\Omega_{\text{eq}} \propto t^{-1/2} \quad (5.10)$$

where Ω_{eq} is the equatorial angular velocity.

Assuming conservation of angular momentum and a certain amount of angular momentum at the solar age for instance one can thus calibrate the law to derive the evolution of the surface velocity from the ZAMS to the present Sun.

This law is now replaced by more realistic prescriptions for the torque due to a magnetized stellar wind. These prescriptions are based on the simple assumption that the stellar surface and the disc are in co-rotation at a specific radius, the Alfvén radius r_A beyond which the wind velocity becomes Alfvénic and the wind is free to flow. Three prescriptions are particularly used, for which the torque depends on the mass and radius of the star, but also on the angular velocity and on the magnetic configuration at the stellar surface. The effect of these prescription on the evolution of surface angular velocity is shown in Fig. 15.

- Kawaler (1988) This analytical prescription is the most popular one.

$$j = -K\Omega\Omega^2 \left(\frac{R}{R_\odot}\right)^{1/2} \left(\frac{M}{M_\odot}\right)^{-1/2} \quad \text{for } \Omega < \Omega_{\text{sat}} \quad (5.11)$$

$$j = -K\Omega\Omega_{\text{sat}}^2 \left(\frac{R}{R_\odot}\right)^{1/2} \left(\frac{M}{M_\odot}\right)^{-1/2} \quad \text{for } \Omega \geq \Omega_{\text{sat}} \quad (5.12)$$

It depends only on the saturation value for rotation, Ω_{sat} , which is associated with a saturation of the stellar magnetic field and usually taken in the range $[8 \Omega_\odot; 20 \Omega_\odot]$. The parameter K is a free parameter that needs to be calibrated on observations. It is typically of the order of 10^{47} . Let us note that Kawaler (1988) actually provides a more general expression in which the mass-loss and the form of the magnetic field configuration are accounted for. The formula of Eq. (5.12) corresponds to the case of a field with a geometry close to the radial geometry (but slightly more complex) and of a total surface field strength that is directly proportional to the rotation rate.

- Reiners & Mohanty (2012)

Very recently, Reiners & Mohanty (2012) proposed a different analytical model for the magnetic torque exerted on late-PMS early main sequence low-mass stars considering that rotation is related to magnetic field strength instead of magnetic flux.

$$\begin{aligned} j &= -C \left[\left(\frac{\Omega}{\Omega_{\text{crit}}}\right)^4 \Omega \left(\frac{R^{16}}{M^2}\right)^{1/3} \right] \quad \text{for } \Omega < \Omega_{\text{crit}} \\ &= -C \left[\Omega \left(\frac{R^{16}}{M^2}\right)^{1/3} \right] \quad \text{for } \Omega \geq \Omega_{\text{crit}} \end{aligned} \quad (5.13)$$

$$\text{with } C \equiv \frac{2}{3} \left(\frac{B_{\text{crit}}^8}{G^2 K_V^4 M}\right)^{1/3} \quad (5.14)$$

with K_V a dimensionless constant scaling factor relating the wind velocity v_A to the Alfvénic velocity : $v_A = K_v \sqrt{GM/r_A}$. This prescription considers

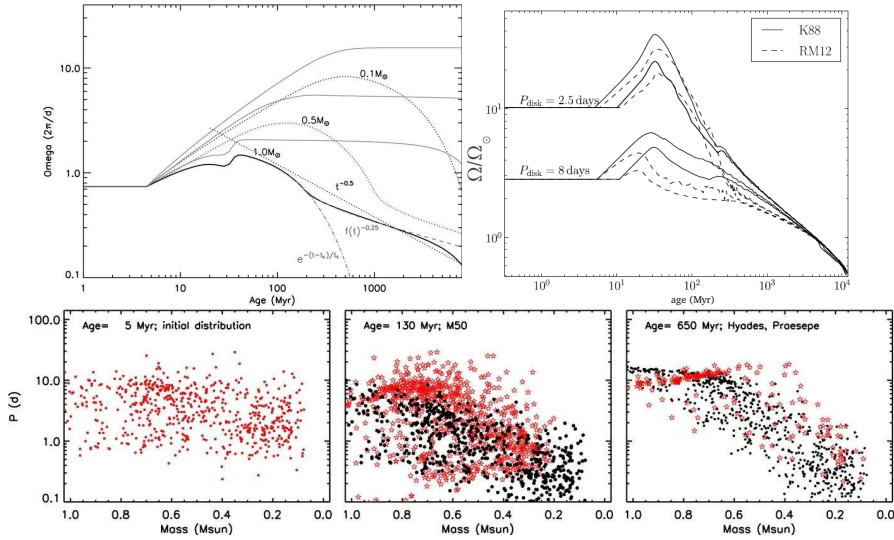


Fig. 15. Upper row - left panel Figure from Reiners & Mohanty 2012 showing the evolution of the surface rotation period from the PMS to several Gyrs for different masses, with (bold black line, dotted lines) and without (solid grey lines) magnetized winds according to Eq. (5.14). Upper row - right panel Figure from Marques & Goupil 2013 showing the impact of using Eq. (5.12) or Eq. (5.14) to describe the torque exerted by the magnetized stellar wind for a $1 M_{\odot}$ model. Lower row Figure from Reiners & Mohanty 2012 showing a comparison between models (in black) and observations (in red) of the rotational period evolution of open clusters stars.

a radial configuration for the magnetic field. It proposes a strong dependence on the stellar radius, making any of its variations having a strong impact on the angular momentum evolution. There also is a strong dependency on Ω_{crit} , which corresponds to the angular velocity for which the magnetic field saturates ($B = B_{\text{crit}}$). This free parameter, together with C , is fitted on observations and the best combination found is $(\Omega_{\text{crit}}, C) = (3\Omega_{\odot}, 2660 g^{5/3} cm^{10/3} s)$

- Matt et al. (2012)

Also in 2012, Matt et al. propose a semi-analytic derivation for the torque resulting from two-dimensional axisymmetric magnetohydrodynamical simulations that compute steady-state solutions for solar-like stellar winds from rotating stars with dipolar magnetic fields. This prescription fits all the simulations to a few percent.

$$\Delta J = K_1^2 B_*^{4m} \dot{M}_W^{1-2m} R_*^{4m+2} \frac{\Omega_*}{(K_2^2 v_{\text{esc}}^2 + \Omega_*^2 R_*^2)^m} \quad (5.15)$$

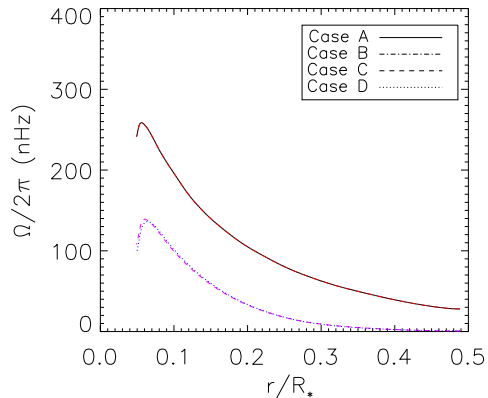


Fig. 16. Mean angular velocity profiles as a function to the reduced radius from 3D hydrodynamical simulations of the inner 50% of the convective envelope of a rotating RGB star with $R \approx 40R_{\odot}$ and $L \approx 400L_{\odot}$, with bulk rotation rates equal to $1/10^{th}$ (cases A and B) and $1/50^{th}$ (cases C and D) of the solar rotation rate 414 nHz. The profiles are obtained by averaging the latitudinal component of the velocity field over latitude, longitude, and time. *From models published in Brun & Palacios (2009).*

where K_2 determines at what spin rate the stellar rotation becomes dynamically important for the wind; K_1 and m are dimensionless fit constants with values of about 1.3 and 0.22 respectively. B_* is the magnetic field strength at the stellar equator, \dot{M}_W is the total mass loss rate, Ω_* the (solid body) angular rotation rate of the stellar surface, M_* and R_* the stellar mass and radius, and v_{esc} is the gravitational escape speed.

5.4 Angular momentum transport in convective regions

As seen in the previous sections, provided the assumption of shellular rotation, it is possible to obtain an elaborate description of the angular momentum transport in the radiative stellar interiors via meridional circulation and shear turbulence. No similar formalism exists for convective regions that are in most cases roughly described by the phenomenological approach of the mixing length theory in 1-D stellar evolution codes.

The problem of how to describe the angular momentum distribution and angular velocity profile in convective regions arose already in the 70s. Tayler (1973) studied the effects of rotation in stellar convective zones and came to the conclusion that meridional currents could develop and alter the rotation law in stellar convective regions. In that case the rotation regime could approach a uniform specific angular momentum in the convective regions ($j \propto r^2\Omega(r)$). Another limiting case would be that of uniform angular velocity profile ($\Omega(r) = const$), and for long no real constrain was available in favour of one or another of these approaches so that the simplest was often adopted, that is uniform angular velocity, e.g. solid-body rotation. The inversion of the solar angular velocity profile from helioseismology later comforted this hypothesis: the Sun presents a fairly uniform *radial* angular velocity within its convective envelope (Kosovichev et al. 1997).

Recent 3-D hydrodynamical simulations of rotating convective envelopes of

stars at different evolutionary stages seem to indicate that not all convective regions behave as the solar one (see for instance Ballot et al. 2007 for young suns). In particular Brun & Palacios (2009) have shown that the extended deep convective envelopes of red giant stars are likely to undergo strong radial differential rotation, with an angular velocity profile of the form $\Omega(r) \propto r^{-0.5}$ (see Fig. 16). Such a change in the adopted angular velocity profile in convective regions in stellar evolution models may impact the angular momentum and the nuclides transport in the underlying radiative region, with possible implications on the surface abundance patterns.

5.5 *The thermal relaxation and the transport loop in Zahn (1992) formalism*

The analysis of the transport loop as generated by meridional circulation and shear turbulence in the framework of Zahn's (1992) formalism allows to disentangle the relative importance of each of the processes at play for the angular momentum transport as well as for the transport of nuclides. This analysis is made easier by the use of the diagnostic tools developed by Decressin et al. (2009).

Here is an overview of the transport loop in typical B-type and F-type main sequence stars, that are summarised in Fig. 17.

B-type star

In B-type stars (and also in O-type stars), no torque is exerted at the surface⁶ although angular momentum losses occur at the surface through the important mass loss. The angular velocity profile is dominated by the angular momentum losses by winds at the surface and by the structural changes of the star during its main sequence evolution (in particular the radius inflation). Meridional circulation develops in the radiative interior that is driven by the local angular momentum transport in the high-density regions, and by shear turbulence in low-density sub-surface regions where a stationary solution is reached and the so-called Gratton-Öpik term ($\propto \bar{\Omega}^2/2\pi G\rho_m$) dominates, forcing the inversion of the angular velocity gradient. *Meridional circulation extracts angular momentum from the core* to compensate for the core contraction and envelope inflation. This extraction is accompanied by the advection of specific entropy, which results in a perturbation of the thermal equilibrium that generate temperature fluctuations on the isobars. *The entropy advection by meridional circulation is compensated by the thermal readjustment.*

The transport of nuclides is on the other hand dominated by the shear turbulence.

Angular momentum and nuclides transport are not dominated by the same processes.

⁶No strong / efficient braking mechanism operates during the main sequence.

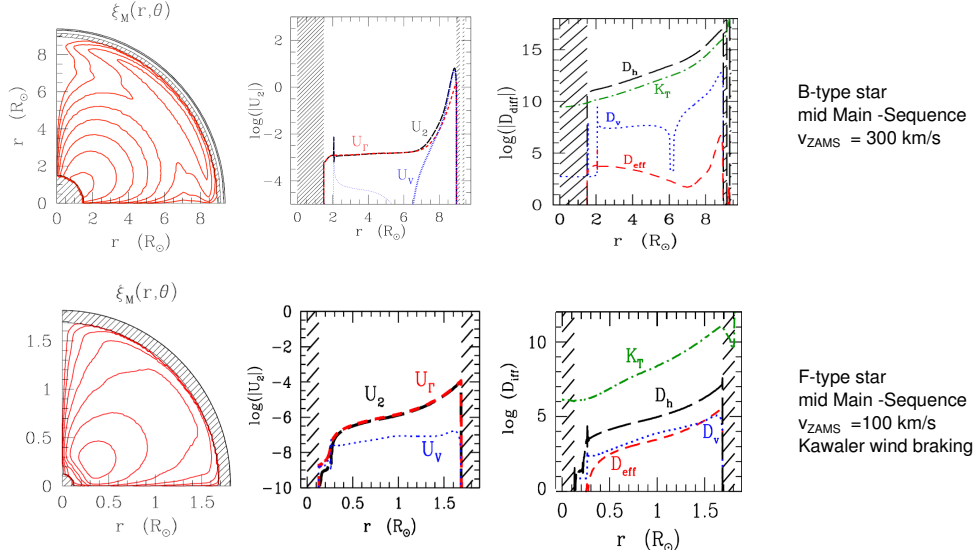


Fig. 17. Transport loop according to Maeder & Zahn (1998) formalism in a typical B-type star (upper row) and in a typical F-type star (lower row). 2-D meridional circulation velocity rendering, meridional circulation velocity U_2 and its two components $U_\Gamma = \frac{5}{4\pi\rho r^4\Omega} \frac{d}{dt} \left[\int_0^{m(r)} r'^2 \bar{\Omega} dm' \right]$ and $U_V = -5\nu_v \partial_r \ln \bar{\Omega}$ and diffusion coefficients (see § 4) are represented on each row when the star is at mid-length on the main sequence ($X_c \approx 0.32$). Adapted from Decressin et al. 2009.

F-type star

F- (and G-)type stars are prone to wind braking during the wTT phase and early main sequence, and this wind is one of the leading mechanisms that shape the internal velocity of the star on the main sequence. Meridional circulation is driven by the local transport of angular momentum everywhere in the radiative interior and the Gratton-Öpik term, associated with the differential rotation rate, is negligible. *Meridional circulation is thus the dominant process for the transport of angular momentum* although it is weakened in the sub-surface regions by the torque exerted by wind braking. This configuration is known as a *wind-driven meridional circulation*, after Zahn (1992). Meridional circulation also extracts angular momentum from the central regions.

The transport of nuclides is in this case due to both meridional circulation and shear turbulence as the diffusion coefficients associated to both mechanisms are of the same order of magnitude.

6 The evolution of rotating stars

In this section I review the main results that have been obtained in the past two decades, following the introduction of rotation and rotation-driven transport processes in stellar evolution codes, with a special emphasis on the models of rotating low-mass stars.

6.1 General trends of rotating stellar evolution models

Stellar evolution models incorporating the transport of angular momentum and chemicals by rotation-driven processes all present the same general trends compared to standard stellar evolution models that are summarized here (see also Maeder & Meynet 2000b, Palacios et al. 2006, Eggenberger et al. 2010, Eggenberger et al. 2012 and references therein) :

- Hydrostatic effects described in § 3 define the evolutionary path of low- and intermediate-mass stars on the PMS and beyond the main sequence: rotating models are more compact and hotter than non-rotating ones;
- Rotation-induced mixing efficiently modifies the hydrogen profile inside main sequence stars so that evolution tracks of moderate to rapid rotators on the Zero Age Main Sequence (ZAMS) are modified. At a given age, rotating models are more luminous and have larger radii, and the main sequence phase duration is longer;
- Rotation-induced transport of nuclides leads to larger cores and longer lifetimes in the different evolutionary stages. For low- and intermediate-mass stars, the red giant branch is bluer and the RGB tip is more luminous in rotating models, which also have larger He core mass;
- Mixing efficiency in terms of nuclides increases with increasing mass and initial rotation, and decreasing metallicity.

Rotation thus affects the stellar parameters not only via the hydrostatic effects that are essentially important during evolutionary phases when the departure from hydrostatic equilibrium is important (PMS, red giant phases), but also through rotation-induced mixing that modifies the elements stratification inside stars and thus impacts lifetimes and core extensions during the main core burning phases.

Rotation modifies stellar evolution and nucleosynthesis from the very early evolutionary phases. Late (post-main sequence) evolutionary phases should always be viewed as the result of the integrated evolution and treated consistently and in continuity with earlier ones.

On top of these general trends, the impact of rotation on the mass and angular momentum losses will be different according to the type of stars and the initial rotation rates. We give hereafter more specific results of rotating stellar evolution models for different stellar types.

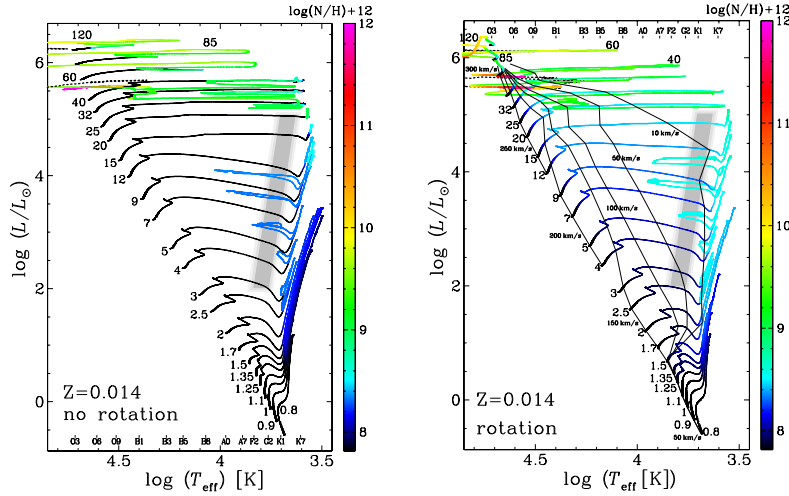


Fig. 18. Evolution of the surface N/H abundance in a grid of rotating (*right*) and non-rotating (*left*) massive stars at solar metallicity ($Z = 0.014$). The models are computed using the advective/diffusive approach. *From Ekström et al. (2012).*

6.2 Massive stars

With the work of the Geneva group and of Pr. N. Langer's group, stellar evolution with rotation has been shown to be successful in efficiently improve the comparison between models' predictions and observational data.

Surface abundance pattern

In massive stars, the high luminosity leads to strong mass-loss and this process is thus an important driver of evolution. We have seen in § 3.3 that the modification of the total potential of the stars and the departure from spherical symmetry induced by rotation modify the radiative transfer and the mass loss of rotating stars, with a larger effect on the most luminous and fastest rotating ones.

Actually, it appears that mass loss is strongly enhanced by rotation for stars with initial masses larger than about $30 M_{\odot}$ and dominates the evolution of the surface abundance pattern during their main sequence evolution. Indeed, the strong mass-loss leads to the exhibition at the surface of regions that have been nuclearly processed through the CNO cycle already on the main sequence. As a consequence, He and N enrichments are predicted from rotating models of O-type stars, in better agreement with observations than the predictions of non-rotating models, as can be seen in Fig. 19. For non-rotating models, the mass-loss is expected to be efficient enough to reveal internal composition only for stars beyond $60 M_{\odot}$.

For stars with masses lower than about $30 M_{\odot}$, mass loss on the main sequence is weaker and does not lead the evolution of the surface abundance pattern that

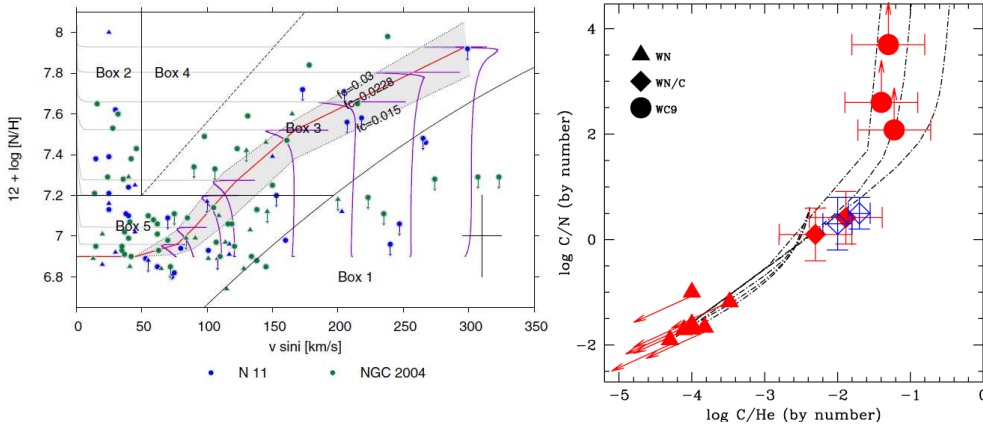


Fig. 19. Left panel – Hunter diagram with N/H as a function of initial rotation velocity; data points are from Hunter et al. (2008a) and evolutionary tracks from Brott et al. (2011a). The grey area corresponds to the predicted values of N/H by models incorporating different mixing efficiency. These models use the diffusive approach for the transport of angular momentum and nuclides (from Brott et al. 2011a). Right panel – C/N versus C/He for a set of Wolf-Rayet stars in WN/C Wolf-Rayet stars in the Galaxy (points) as compared to rotating models by Meynet & Maeder (2005) (from Martins et al. 2007).

is largely influenced by the rotation-driven transport processes, and in particular by the shear turbulence that dominates the transport of nuclides on the main sequence.

The shear allows to connect the surface to regions nuclearly processed through the CNO cycle : nitrogen and to a lesser extent helium are enhanced at the surface while carbon is depleted. These abundance variations are also expected in non-rotating stars but will only appear during the later red supergiant phase when mass loss has uncovered inner processed regions. In this mass range, the earlier nitrogen enhancement predicted by rotating models also improves the comparison with observations (Fig. 19).

As can be seen from Fig. 18 and Fig. 20, these features are qualitatively found using different approaches both for the transport of angular momentum and nuclides and for the mass loss, but substantial differences arise from one grid of models to another as can be seen in Fig. 20 extracted from Chieffi & Limongi (2013). These differences are partly due to different input standard physics (different initial chemical composition, different treatment of mass loss) but are also the result of different treatment of rotation and rotation-induced transport processes (see Brott et al. 2011a, Ekström et al. 2012, Chieffi & Limongi 2013).

Number populations

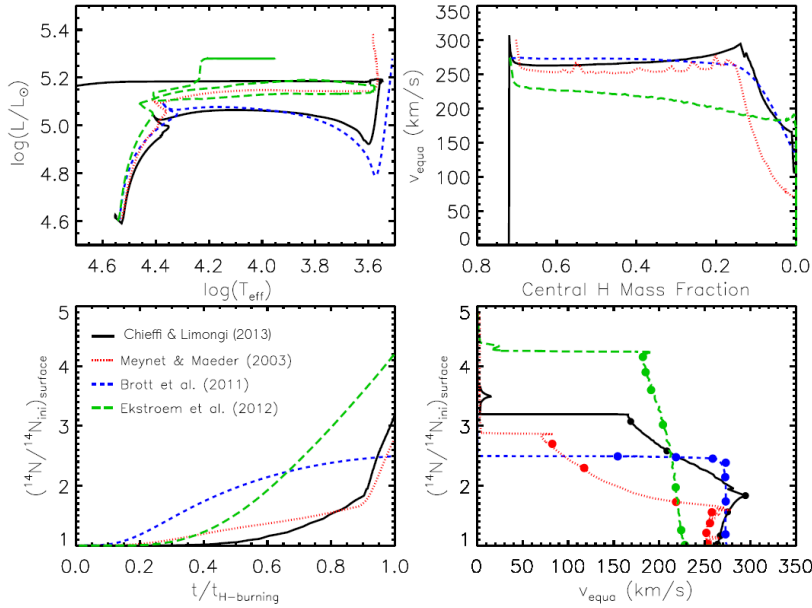


Fig. 20. HR diagram, surface velocity evolution as a function of central hydrogen mass fraction, surface nitrogen relative enhancement as a function of time on the main sequence and of surface velocity for $20 M_{\odot}$ models from 4 different sources as listed on the diagram. The initial velocities and chemical compositions slightly differ from one to another as well as the treatment of rotational transport and mass loss. *From Chieffi & Limongi 2013 (see paper for more details).*

The number counts of different Wolf-Rayet stars (different subtypes) as well as that of blue and red supergiants as revealed by the observational census has been a long standing problem because the picture drawn by standard stellar evolution models is far from reproducing it (Langer & Maeder 1995, Meynet & Maeder 2003). Including rotation in single stellar evolution models has greatly improved the comparison as direct consequence of the mass-loss enhancement and mixing described just above as shown in Fig. 21. Rotation modifies the evolutionary sequence of massive stars in terms of spectral types and leads to a better yet not completely good agreement with observations. In particular the number of Wolf-Rayet stars predicted by models including rotation is larger, with a significant lowering of the minimum initial mass that a star should have to enter this phase.

6.3 Low and intermediate mass stars beyond the ZAMS

The introduction of rotation-driven transport in stellar evolution codes, and more notably using the exact same parameters for the shear turbulence modelling as

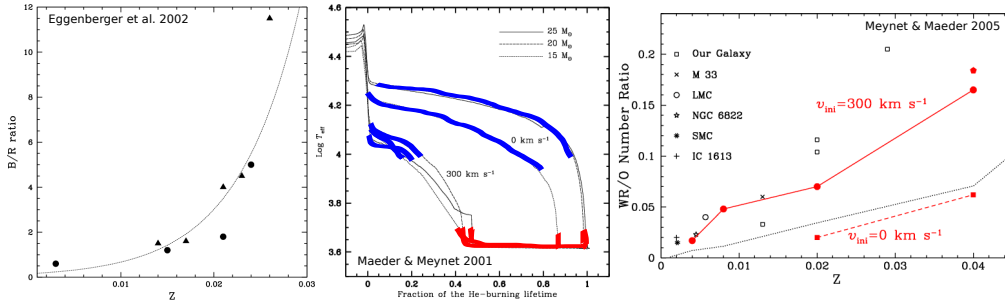


Fig. 21. Blue to red supergiants number counts in young open clusters of the Galaxy and in the SMC; model predictions with and without rotation for different masses at the metallicity of the SMC, with the blue and the red supergiant phases highlighted; proportion of Wolf-Rayet to O-type stars at different metallicities and predictions from rotating and non-rotating models.

those successfully employed for massive stars⁷, also yields significant improvement of the comparison between models and observations.

The rotation profile of the Sun

Helioseismology has revealed that the bulk of the solar radiative interior rotates almost as a solid body (Kosovichev et al. 1997, see also Fig. 3), a profile that cannot be reproduced when shear turbulence and meridional circulation are the only efficient mechanisms to transport angular momentum.

Adding the transport by the IGW generated at the base of the solar convective envelope, Charbonnel & Talon (2005) have shown that they efficiently extract angular momentum from the solar interior, flattening out the rotation profile built by meridional circulation and shear turbulence. IGW associated to rotation-driven instabilities can thus be viewed as efficient transport processes of angular momentum in solar type stars and propose a possible solution to this long-standing puzzle. Concomitantly, Eggenberger et al. (2005) have shown that magnetic fields could also enforce near solid-body rotation in the solar radiative interior, and more recently, the addition of g-mode candidates to the inversion of the solar angular velocity profile reveal a possible acceleration of the solar core (García et al. 2011, see also Fig. 3a), showing that this question is still to be fully understood.

Rotation of red giant stars

The rotation of red giants is constrained by $v \sin i$ spectroscopic determinations and by the inversion of mixed gravity/pressure modes from asteroseismology

⁷This is only valid when the advective/diffusive formalism is used. In the diffusive formalism, the parameters tuning depends on the type of stars studied.

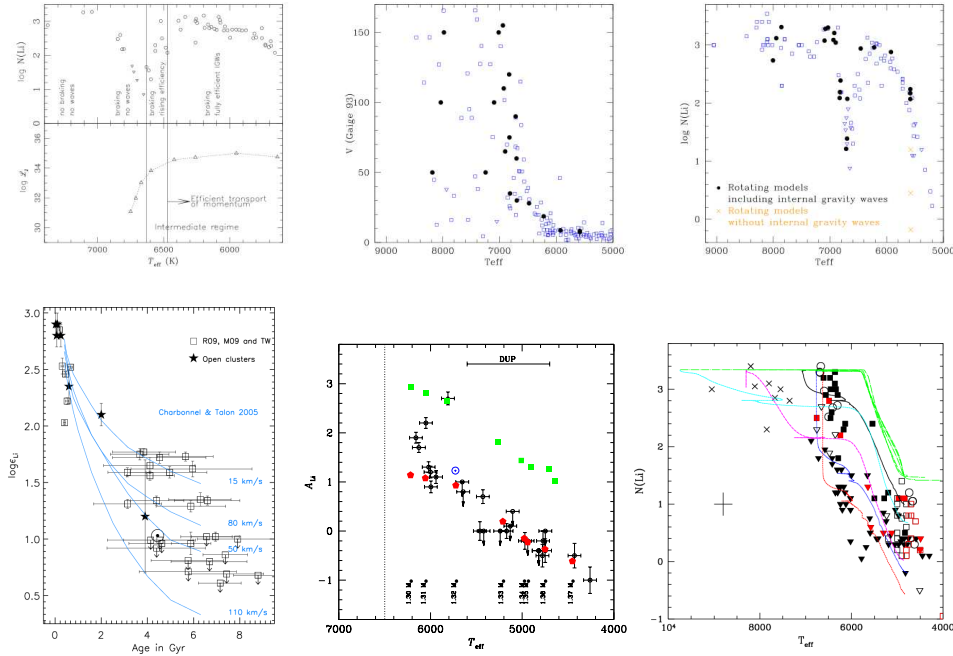


Fig. 22. Successes of stellar evolution models including rotation-driven transport and IGW to reproduce Li abundances in various environments. Upper row: The Lithium dip revisited with models including rotation-driven instabilities and IGW. The waves luminosity, the calibrated surface velocities based on Gaigé (1993), and the resulting surface lithium abundances are displayed together with observational data for models in the mass range. (From Charbonnel & Talon 2008). Lower row Left : Lithium abundance as a function of age for solar twins with over-plotted predicted evolution from Charbonnel & Talon 2005 (From Baumann et al. 2012); Middle : Lithium abundance as a function of effective temperature for subgiant stars in the M67 open cluster compared to models with rotational mixing and no IGW for two different initial rotation velocities (From Canto Martins et al. 2011). Right : Comparison of stellar evolution predictions for models without rotation (green) and with rotation (other colors) belonging to the hot side of the Li-dip on the main sequence and that evolve on the subgiant branch. Data are for single stars from open clusters and the galactic field (From Palacios et al. 2003).

data as pointed out in § 2. These stars present slow projected surface velocities and internal differential rotation, both characteristics qualitatively predicted by models including rotation (Palacios et al. 2006), but quantitatively far from the observed values. Indeed, the models including the transport processes described in the previous section predict a steep decrease of the surface velocity driven by the expansion of the stellar radius that basically dominates the transport of angular momentum in the very limited radiative interiors of red giants. This is valid under

seemingly abusive assumption of solid-body rotation in the very extended (up to 90% of the total stellar radius) and should be emphasized if differential rotation of the convective envelope is considered, as suggested by 3D hydrodynamical simulations (Brun & Palacios 2009, see also Fig. 16). In addition to that, Palacios et al. (2006) and Eggenberger et al. (2012b) have shown that the models including self-consistent transport of angular momentum in radiation interiors predict much steeper angular velocity profiles than that derived from asteroseismic data by Deheuvels et al. (2012) (Fig. 3b).

This discrepancy between models and observations for red giant stars points towards additional angular momentum transport processes that could efficiently redistribute angular momentum in these stars, accelerating the surface and decelerating the core. Planets accretion has been suggested recently by Carlberg et al. (2012) as one of the possible causes for rapid rotation of low-mass red giants, but no exploration of such processes have been made with stellar evolution models so far.

Lithium abundance

For low- and intermediate-mass stars, introducing rotation-driven transport processes and IGW allows to build a self-consistent picture for the Li surface abundance evolution in various environments, as can be seen in Fig. 22.

In stars with shallow convective envelopes on the main sequence, IGW are inefficient in the transport of angular momentum and chemicals, which is dominated by meridional circulation and turbulent shear. The degree of mixing affecting the Li surface abundance depends on the degree of radial differential rotation which feeds the shear. This is directly linked to the surface rotation rate and to the torque applied at the surface by the magnetized winds that these stars experience during their early evolution on the main sequence. By calibrating it on the observed rotation rates of low-mass stars in open clusters such as the Hyades (the calibration concerns the constants that are introduced in the wind braking prescriptions described in § 5.3), Palacios et al. (2003) and Canto Martins et al. (2011) have shown that the shear mixing efficiently operates on the main sequence, leading to lithium abundance reduction at the stellar surface as the star evolves on the main sequence and beyond, in excellent agreement with observations.

In cooler and lower-mass stars, the convective envelope on the main sequence is deep enough for the IGW to play a significant part in the transport of angular momentum and (indirectly) that of nuclides. The lithium dip showed in upper left panel of Fig. 22 is a characteristic feature of lithium abundances which is seen both in the field and in open clusters (e.g., Wallerstein et al. 1965; Boesgaard & Tripicco 1986; Balachandran 1995). It corresponds to a narrow region in effective temperature (around $T_{\text{eff}} \sim 6650$ K) where the surface Li abundances are reduced by up to ~ 2.5 dex. While models including rotation-driven transport for stars on the hot side of the dip (more massive than about $1.35 M_{\odot}$) lead to important lithium (and beryllium) destruction at the correct T_{eff} (Talon & Charbonnel 1998, Palacios et al. 2003), they predict even larger Li de-

pletion for stars on the red cold side of the dip, contrary to what is observed. When IGW are also taken into account for the transport of angular momentum in these models, as they should be, they appear to significantly reduce the shear mixing, thus partially preventing Li depletion, in agreement with observations (Charbonnel & Talon 2005). Moreover, these models also reproduce correctly further evolution of Li surface abundances of low-mass main sequence stars in open clusters (lower left panel of Fig. 22).

CNO abundances

The successes in reproducing abundance patterns of CNO with rotating models is limited to A- and F- main sequence stars. For these stars contrary to models solely including microscopic diffusion of nuclides, rotation-driven mixing inhibits CNO atomic diffusion in the temperature range of the Li dip, in agreement with observations (Palacios et al. 2003, Varenne & Monier 1999, Takeda et al. 1998). On the other hand, the carbon depletion and carbon isotopic ratio decrease associated with the increase of nitrogen abundances in red giant stars that was tentatively considered a result of rotation-driven transport of nuclides connecting regions where the CN-cycle operates to the stellar surfaces, cannot be reproduced by models of the diffusive/advective type (Palacios et al. 2006). These abundances variations are attributed to thermohaline mixing occurring in these hydrogen shell burning stars (Charbonnel & Lagarde 2010) .

6.4 Solar-type stars on the PMS

To close this overview, let us turn to the angular momentum evolution of young (pre-main sequence and early-main sequence) solar-type stars for which a large number of rotation periods have been measured (see Figs 2 and 15) in clusters with ages ranging from 1 Myr to 1 Gyr and can serve to elucidate the dominant processes controlling the angular velocity evolution from the “*disc-locking*” phase to the early-main sequence.

HR diagram

As explained earlier (see § 6.1), the hydrostatic effects (e.g. the mechanical and thermal distortion associated with rotation) dominate the impact of rotation on the evolutionary path of low-mass stars on the pre-main sequence. Rotation globally lowers gravity and makes the star appear as if it was a less massive non-rotating one as can be seen in Fig. 23. The transport of angular momentum and chemicals do not modify the evolutionary path, yet they obviously impact the surface rotation and chemical pattern. The more rapid the rotation at disc decoupling, the larger the shift between non-rotating and rotating tracks.

On the main sequence, apart from the slight shift of the ZAMS inherited from the PMS different evolution, no noticeable difference on the tracks is expected (see Pinsonneault et al. 1989, Eggenberger et al. 2012).

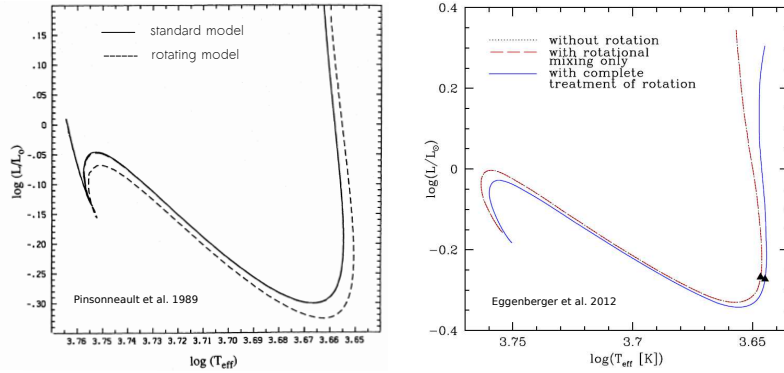


Fig. 23. Hertzsprung diagram for rotating and non-rotating models of a $1 M_{\odot}$ star including both the hydrostatic effects described in § 3 and rotational transport using the diffusive approach (left panel) and the advective/diffusive approach (right panel).

Lithium abundance

Lithium nuclear burning occurs during the PMS as soon as temperature above $2.5 \cdot 10^6$ K can be reached inside the star. These temperatures are reached when the star is still fully convective, so that the destruction of lithium in the core regions immediately shows up at the surface. When the radiative core appears, Li burning may still be going on but in the absence of any transport mechanisms in the radiative interior to connect the now receding convective envelope, Li surface abundance is expected to remain constant. When rotational mixing is taken into account, Mendes (1999), Eggenberger et al. (2012), and Marques & Goupil (2013) obtain an additional surface Li depletion (as expected if the rotational mixing is efficient) that remains marginal (does not exceed 0.25 dex according to Eggenberger et al. 2012).

An important point made by Marques & Goupil (2013) is that despite the small effect on the PMS, rotation may significantly affect the evolution of the lithium abundance further at the ZAMS and beyond, depending on the initial conditions and particularly on the assumed rotation period during the CTT (disc-locking) phase. This effect is seemingly due to the gradients of angular velocity hence the amount of shear that can develop in the radiative regions where Li is being processed. It is thus crucial to properly account for rotation-induced transport during the early phases.

Surface angular velocity

The surface angular velocity evolution during the PMS of solar-type stars is first controlled by the so-called *disc-locking*, and the rotation period is imposed in stellar evolution codes so as to best fit the data from young open clusters.

The duration of this phase is not completely established and could vary between 3 and 6 to 9 Myrs for solar-type stars according to the initial velocity (see Irwin & Bouvier 2009, Gallet & Bouvier 2013). During that time, the *surface angular velocity* $\Omega_{\text{eq,surf}}$ is maintained constant while the star rapidly contracts. Models indicate that for longer disc-locking phases, the angular velocity at the ZAMS is slower. Once the disc-locking phase is over, the constant surface angular velocity constrain is released, the surface of the star is spun up due to the global reduction of the stellar radius and to the now quasi-conservation of angular momentum. The later the disc-decoupling occurs, the less contraction is expected and so the less spin up. On the other hand, the magnetized winds (see § 5.3) will also act during this phase and prior to the arrival on the ZAMS, and limit the spin-up of the surface.

The evolution of the surface angular velocity from the disc decoupling to the ZAMS is shown in Fig. 24 where we show the internal rotation profiles at different ages for models only including rotation hydrostatic effects and rotation-driven transport and for models additionally including the transport by IGW (Charbonnel et al. 2013).

Internal rotation profile

When the transport by IGW in the radiative interior is neglected (which should not be done as we shall show below), the meridional circulation and the hydrostatic terms control the transport of angular momentum and build up of differential rotation with a negative gradient of angular velocity (the core rotates faster than the surface). When the surface constrain is released after disc decoupling, the surface is spun up but the transport and the core contraction are efficient enough to maintain and even exacerbate the differential rotation as can be seen on the left panel of Fig. 24.

According now to what has been explained in § 4.3, IGW are likely to be efficient to transport angular momentum during the PMS evolution, and it is actually the case as soon as the radiative core appears in the star and the waves have a radiative region to propagate and dissipate into. The low-degree, low-frequency waves are those experiencing the largest Doppler shift due to differential rotation and they penetrate deep in the core regions where they deposit negative angular momentum, thus efficiently spinning down these regions as can be seen on the right panel of Fig. 24. On the other hand, closer to the surface the angular velocity gradient is not modified so that the effect of IGW cannot be detected by confronting rotation periods.

Such rotation profiles however will imply a radically different evolution for the further evolution beyond the ZAMS, in particular when the effect of the magnetized winds will be at its maximum.

IGW dominate the transport of angular momentum in solar-type PMS stars and strongly spin down the central regions as the stars evolve

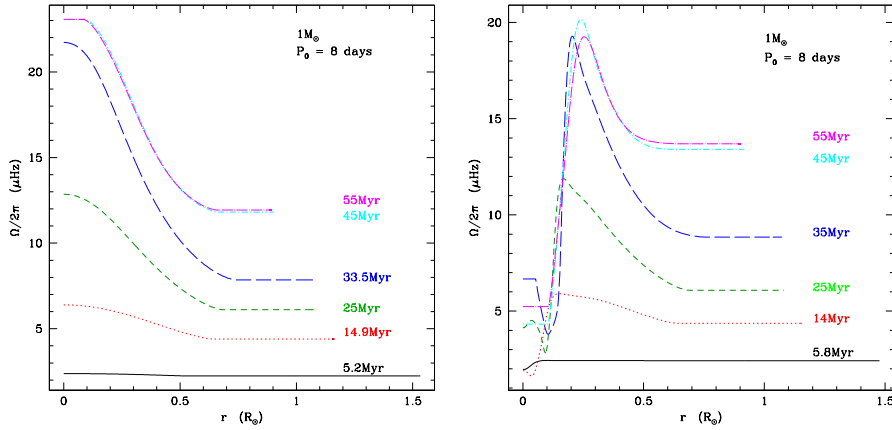


Fig. 24. Evolution of the internal rotation profile of a $1 M_{\odot}$ at solar metallicity with a rotation period of 8 days during the disc-locking phase, and an initial velocity of about 40% of the critical velocity, that is to say $v \approx 12 \text{ km.s}^{-1}$. **Left panel** Case where IGW are neglected; **Right panel** Case with rotation-driven transport and IGWs. *From Charbonnel et al. 2013.*

to the ZAMS. The slope inversion of the angular velocity profile and the peculiar configuration with a core rotating slower than the surface needs to be taken into account to study and understand the rotation and chemical evolution of these stars on the early main sequence.

I sincerely thank the organizers of this school for trusting my pedagogical abilities and giving me the opportunity to present this lecture. I also thank the STAREVOL team members without whom such a document could not have been published, with a special thought to M. Forestini, the TOUPIES team and J. Bouvier, and F. Martins for fruitful discussions on massive stars.

References

- Abney, W. D. W. 1877, MNRAS, 37, 278
 Abt, H. A., Levato, H., & Grosso, M. 2002, ApJ, 573, 359
 Acheson D.J., 1978, Phil. Trans. Roy. Soc. Lond. A289, 459
 Alvan, L., Brun, A. S., & Mathis, S. 2012, SF2A-2012: Proceedings of the Annual meeting of the French Society of Astronomy and Astrophysics, 289
 Balachandran, S. 1995, ApJ, 446, 203
 Ballot, J., Brun, A. S., & Turck-Chièze, S. 2007, ApJ, 669, 1190
 Baraffe, I., Chabrier, G., & Gallardo, J. 2009, ApJL, 702, L27
 Barnbaum, C., Morris, M., & Kahane, C. 1995, ApJ, 450, 862
 Baumann, P., Ramírez, I., Meléndez, J., Asplund, M., & Lind, K. 2010, A&A, 519, A87
 Bazan, G., Dearborn, D. S. P., Dossa, D. D., Eggleton, P. P., et al. 2003, 3D Stellar Evolution, ASP Conf. Series vol 293

- Beck, P. G., Montalbán, J., Kallinger, T., et al. 2012, *Nature*, 481, 55
- Boesgaard, A. M., & Krugler Hollek, J. 2009, *ApJ*, 691, 1412
- Boesgaard, A. M. 2005, *Cosmic Abundances as Records of Stellar Evolution and Nucleosynthesis*, 336, 39
- Boesgaard, A. M., Deliyannis, C. P., & Steinhauer, A. 2005, *ApJ*, 621, 991
- Boesgaard, A. M. 1989, *ApJ*, 336, 798
- Boesgaard, A. M., & Tripicco, M. J. 1986, *ApJ*, 303, 724
- Böhm-Vitense, E. 1958, *ZA*, 46, 108
- Bragança, G. A., Daflon, S., Cunha, K., et al. 2012, *AJ*, 144, 130
- Brott, I., Evans, C. J., Hunter, I., et al. 2011 b, *A&A*, 530, A116
- Brott, I., de Mink, S. E., Cantiello, M., et al. 2011 a, *A&A*, 530, A115
- Brun, A. S., & Palacios, A. 2009, *ApJ*, 702, 1078
- Canto Martins, B. L., Lèbre, A., Palacios, A., et al. 2011, *A&A*, 527, A94
- Canuto, V. M. 1998, *ApJ*, 508, 767
- Carlberg, J. K., Cunha, K., Smith, V. V., & Majewski, S. R. 2012, *ApJ*, 757, 109
- Carlberg, J. K., Majewski, S. R., Patterson, R. J., et al. 2011, *ApJ*, 732, 39
- Chaboyer, B., & Zahn, J.-P. 1992, *A&A*, 253, 173
- Chandrasekhar S., 1961, *Hydrodynamic and Hydromagnetic Stability*, Oxford Univ. Press
- Canto Martins, B. L., Lèbre, A., Palacios, A., et al. 2011, *A&A*, 527, A94
- Charbonnel, C., Decressin, T., Amard, L., Palacios, A. & Talon, S. 2013, *A&A*, 554, A40
- Charbonnel, C., & Lagarde, N. 2010, *A&A*, 522, A10
- Charbonnel, C., & Talon, S. 2008, *IAU Symposium*, 252, 163
- Charbonnel, C., & Talon, S. 2005, *Science*, 309, 2189
- Charbonnel, C., & Balachandran, S. C. 2000, *A&A*, 359, 563
- Chieffi, A., & Limongi, M. 2013, *ApJ*, 764, 21
- Clayton, D. D. 1984, *Principles of stellar evolution and nucleosynthesis..* D. D. Clayton. 2nd edition. The University of Chicago Press, Chicago - London. 612 pp. Price 15.00 (1984).
- Cranmer, S. R., & Saar, S. H. 2011, *ApJ*, 741, 54
- Decressin, T., Mathis, S., Palacios, A., et al. 2009, *A&A*, 495, 271
- Deheuvels, S., García, R. A., Chaplin, W. J., et al. 2012, *ApJ*, 756, 19
- de Medeiros, J. R. 2004, *Stellar Rotation*, 215, 144
- De Ridder, J., Barban, C., Baudin, F., et al. 2009, *Nature*, 459, 398
- Eddington, A. S. 1925, *The Observatory*, 48, 73
- Eggenberger, P., Montalbán, J., & Miglio, A. 2012, *A&A*, 544, L4
- Eggenberger, P., Haemmerlé, L., Meynet, G., & Maeder, A. 2012, *A&A*, 539, A70
- Eggenberger, P., Miglio, A., Montalbán, J., et al. 2010, *A&A*, 509, A72
- Eggenberger, P., Meynet, G., Maeder, A., et al. 2008, *Ap&SS*, 316, 43
- Eggenberger, P., Maeder, A., & Meynet, G. 2005, *A&A*, 440, L9
- Eggenberger, P., Meynet, G., & Maeder, A. 2002, *A&A*, 386, 576
- Ekström, S., Georgy, C., Eggenberger, P., et al. 2012, *A&A*, 537, A146
- Endal, A. S., & Sofia, S. 1978, *ApJ*, 220, 279

- Endal, A. S., & Sofia, S. 1976, *ApJ*, 210, 184
- Espinosa Lara, F., & Rieutord, M. 2011, *A&A*, 533, A43
- Fowler, A. 1900, *MNRAS*, 60, 579
- Frebel, A., Aoki, W., Christlieb, N., et al. 2005, *Nature*, 434, 871
- Fricke K.J., 1968, *Z. Astrophys.*, 68, 317
- Galilei, G., Welsler, M., & de Filiis, A. 1613, Roma, G. Mascadi, 1613.
- Gallet, F. & Bouvier, J. 2013, *A&A*, in press
- García, R. A., Salabert, D., Ballot, J., et al. 2011, *Journal of Physics Conference Series*, 271, 012046
- Goldreich P., Murray N., Kumar, P., 1994, *ApJ* 424, 466
- Goldreich P., Schubert G., 1967, *ApJ* 150, 571
- Gratton, R. G., Sneden, C., Carretta, E., & Bragaglia, A. 2000, *A&A*, 354, 169
- Heap, S. R., Lanz, T., & Hubeny, I. 2006, *ApJ*, 638, 409
- Heger, A., Langer, N., & Woosley, S. E. 2000, *ApJ*, 528, 368
- Herwig, F., Freytag, B., Hueckstaedt, R. M., & Timmes, F. X. 2006, *ApJ*, 642, 1057
- Hunter, I., Brott, I., Lennon, D. J., et al. 2008a, *ApJL*, 676, L29
- Hunter, I., Lennon, D. J., Dufton, P. L., et al. 2008b, *A&A*, 479, 541
- Irwin, J., & Bouvier, J. 2009, *IAU Symposium*, 258, 363
- Kawaler, S. D. 1988, *ApJ*, 333, 236
- Kippenhahn, R., & Thomas, H.-C. 1970, *IAU Colloq. 4: Stellar Rotation*, 20
- Kippenhahn, R., & Weigert, A. 1990, *Stellar Structure and Evolution*, XVI, 468 pp. 192 figs.. Springer-Verlag Berlin Heidelberg New York. Also *Astronomy and Astrophysics Library*,
- Knobloch E., Spruit H.C. 1983, *A&A* 125, 59
- Kopal, Z. 1959, *The International Astrophysics Series*, London: Chapman & Hall, 1959
- Kosovichev, A. G., Schou, J., Scherrer, P. H., et al. 1997, *Sounding Solar and Stellar Interiors*, 181, 203
- Langer, N., & Maeder, A. 1995, *A&A*, 295, 685
- Lèbre, A., Palacios, A., Do Nascimento, J. D., Jr., et al. 2009, *A&A*, 504, 1011
- Lucy, L. B. 1967, *ZA*, 65, 89
- Maeder, A. 2009, *Physics, Formation and Evolution of Rotating Stars: , Astronomy and Astrophysics Library*. ISBN 978-3-540-76948-4. Springer Berlin Heidelberg, 2009
- Maeder A., 2003, *A&A*, 399, 263
- Maeder, A., & Meynet, G. 2000, *A&A*, 361, 159
- Maeder, A., & Meynet, G. 2000, *ARA&A*, 38, 143
- Maeder, A. 1999, *A&A*, 347, 185
- Maeder, A., & Zahn, J.-P. 1998, *A&A*, 334, 1000
- Maeder, A. 1997, *A&A*, 321, 134
- Marques, J. P., Goupil, M. J., Lebreton, Y., et al. 2013, *A&A*, 549, A74
- Marques, J. P., & Goupil, M. J. 2013, *Lecture Notes in Physics*, Berlin Springer Verlag, 865, 75
- Martin, E. L., & Claret, A. 1996, *A&A*, 306, 408
- Martins, F., Hillier, D. J., Bouret, J. C., et al. 2009, *A&A*, 495, 257

- Martins, F., Genzel, R., Hillier, D. J., et al. 2007, *A&A*, 468, 233
- Mathis, S., & de Brye, N. 2012, *A&A*, 540, A37
- Mathis S., Palacios A., Zahn J.-P., 2004, *A&A* 425, 243
- Matt, S. P., MacGregor, K. B., Pinsonneault, M. H., & Greene, T. P. 2012, *ApJL*, 754, L26
- Mendes, L. T. S. 1999, Ph.D. Thesis,
- Meynet, G., & Maeder, A. 2005, *A&A*, 429, 581
- Meynet, G., & Maeder, A. 2003, *A&A*, 404, 975
- Meynet, G., Ekstrom, S., Maeder, A., et al. 2013, *Lecture Notes in Physics*, Berlin Springer Verlag, 865, 3
- Meynet, G., & Maeder, A. 1997, *A&A*, 321, 465
- Mishenina, T. V., Soubiran, C., Kovtyukh, V. V., Katsova, M. M., & Livshits, M. A. 2012, *A&A*, 547, A106
- Mokiem, M. R., de Koter, A., Evans, C. J., et al. 2006, *A&A*, 456, 1131
- Monck, W. H. S. 1890, *The Observatory*, 13, 180
- Mosser, B., Goupil, M. J., Belkacem, K., et al. 2012b, *A&A*, 548, A10
- Mosser, B., Goupil, M. J., Belkacem, K., et al. 2012a, *A&A*, 540, A143
- Palacios, A., Charbonnel, C., Talon, S., & Siess, L. 2006, *A&A*, 453, 261
- Palacios, A., Talon, S., Charbonnel, C., & Forestini, M. 2003, *A&A*, 399, 603
- Palla, F., & Stahler, S. W. 1993, *ApJ*, 418, 414
- Palla, F., & Stahler, S. W. 1992, *ApJ*, 392, 667
- Pantillon, F. P., Talon, S., & Charbonnel, C. 2007, *A&A*, 474, 155
- Paxton, B., Cantiello, M., Arras, P., et al. 2013, *arXiv:1301.0319*
- Penny, L. R., & Gies, D. R. 2009, *ApJ*, 700, 844
- Penny, L. R. 1996, *ApJ*, 463, 737
- Pinsonneault, M. H., Kawaler, S. D., Sofia, S., & Demarque, P. 1989, *ApJ*, 338, 424
- Potter, A. T. 2012, Ph.D. Thesis,
- Reimers, D. 1975, *Memoires of the Societe Royale des Sciences de Liege*, 8, 369
- Reiners, A., & Mohanty, S. 2012, *ApJ*, 746, 43
- Richard D. & Zahn J.-P., 1999, *A&A*, 347, 734
- Rieutord, M., & Espinosa Lara, F. 2013, *Lecture Notes in Physics*, Berlin Springer Verlag, 865, 49
- Rieutord, M. 2008, *EAS Publications Series*, 21, 127
- Rogers, T. M., Glatzmaier, G. A., & Jones, C. A. 2006, *ApJ*, 653, 765
- Royer, F., Zorec, J., & Gómez, A. E. 2007, *A&A*, 463, 671
- Rucinski, S. M. 1990, *PASP*, 102, 306
- Saar, S. H. 1996, *Stellar Surface Structure*, 176, 237
- Siess, L., Forestini, M., & Bertout, C. 1999, *A&A*, 342, 480
- Siess, L., Forestini, M., & Bertout, C. 1997, *A&A*, 326, 1001
- Siess, L., & Forestini, M. 1996, *A&A*, 308, 472
- Skumanich, A. 1972, *ApJ*, 171, 565
- Souleyre, A. 1898, *Bulletin de la Societe Astronomique de France et Revue Mensuelle d'Astronomie, de Meteorologie et de Physique du Globe*, 12, 304

- Takeda, Y., Kawanomoto, S., Takada-Hidai, M., & Sadakane, K. 1998, PASJ, 50, 509
- Talon, S. 2008, EAS Publications Series, 32, 81
- Talon, S., & Charbonnel, C. 2008, A& A, 482, 597
- Talon, S., & Charbonnel, C. 2005, A& A, 440, 981
- Talon, S., & Charbonnel, C. 2003, A&A, 405, 1025
- Talon, S., & Charbonnel, C. 1998, A&A, 335, 959
- Talon S., Zahn J.-P., 1997, A&A 317, 749
- Tayler, R. J. 1973, MNRAS, 165, 39
- Tout, C. A., Livio, M., & Bonnell, I. A. 1999, MNRAS, 310, 360
- Turcotte, S., Keller, S. C., & Cavallo, R. M. 2003, 3D Stellar Evolution, ASP Conf. Series vol 293
- Unno W., Osaki Y., Ando H., Saio H., Shibahashi H., 1989, "Nonradial oscillations of stars", 2nd edition, University of Tokyo Press
- Varenne, O., & Monier, R. 1999, A&A, 351, 247
- Vogt H., 1925, Astron. Nachr. 223, 229
- von Zeipel, H. 1924, MNRAS, 84, 665
- Walborn, N. R., Maíz Apellániz, J., Sota, A., et al. 2011, AJ, 142, 150
- Wallerstein, G., Herbig, G. H., & Conti, P. S. 1965, ApJ, 141, 610
- Yoon, S.-C., & Langer, N. 2005, A&A, 443, 643
- Zahn, J.-P., Talon, S., & Matias, J. 1997, A&A, 322, 320
- Zahn, J.-P. 1992, A&A, 265, 115
- Zeng, Y. R. 2002, A&A, 394, 965
- Zhao, M., Monnier, J. D., & Che, X. 2011, IAU Symposium, 272, 44